

Sebastian Schneider, BSc

Attitude Estimation of (defunct) Satellites using Bi-static Satellite Laser Ranging Simulations

MASTER'S THESIS

to achieve the university degree of

Diplom-Ingenieur

Master's degree programme:

Space Sciences and Earth from Space

submitted to

Graz University of Technology

Supervisor

Sandro Krauß, Ass.Prof. Dipl.-Ing. Dr.techn. Bakk.techn.

Institute of Geodesy

Graz, November 2024

Abstract

This thesis analyzes the potential of a method for determining the attitude of satellites and space debris using bistatic Satellite Laser Ranging (SLR) simulations. The target of removing defective satellites from orbit is supported in an essential way by the ability to measure their rotational characteristics from ground. The superior precision of SLR allows for an identification of the individual Corner Cube Reflectors (CCR) on a spacecraft's surface within the SLR data. The true distance between two reflectors is known from the arrangement on the satellite or is defined in the simulation. Three CCRs in a line at different distances is a suitable pattern for this method. One CCR is assumed to be in the origin while the position of the others momentarily remain unknown. The objective is to estimate the position of a second CCR in space relative to the first. An unknown attitude limits the area of the potential position to a spherical surface around the first CCR. SLR range measurements yield the range difference between the CCRs in observation vector direction. Thus, a plane can be defined which is perpendicular to the observation vector and shifted by the range difference. The intersection of the sphere and the plane produces a circle of potential positions for the second CCR. Once simultaneous SLR data is available from the second SLR station the circular region is further refined to two potential points in space, by the intersection of the two circles. The two CCRs can now be connected with a surface vector, which can subsequently be used to reconstruct the attitude of this vector over time. Within this thesis the theoretical limits of this method are investigated. The technique can also be applied to a larger number of CCRs, knowing their true arrangement and provided that at least two CCR can be identified.

Kurzfassung

In dieser Arbeit wird das Potenzial einer Methode zur Lagebestimmung von Satelliten und Weltraummüll mittels bistatischer Satellite Laser Ranging (SLR)-Simulationen analysiert. Das Ziel, defekte Satelliten aus der Umlaufbahn zu entfernen, wird durch die Möglichkeit unterstützt, die Rotation vom Boden aus zu messen. Die Präzision von SLR ermöglicht die Identifizierung der einzelnen Corner-Cube-Reflektoren (CCR) in den SLR-Daten. Der tatsächliche Abstand zwischen zwei CCRs ist bekannt oder wird in der Simulation definiert. Drei CCRs in einer Reihe mit unterschiedlichen Abständen sind ein geeignetes Muster für diese Methode. Es wird angenommen, dass sich ein CCR im Ursprung befindet, während die Position der anderen vorerst unbekannt bleibt. Ziel ist es, die Position eines zweiten CCR im Raum relativ zum ersten zu berechnen. Die unbekannte Lage des Satelliten schränkt den Bereich der möglichen Position auf eine Kugeloberfläche um den ersten CCR ein. SLR Messungen liefern die Entfernungsdifferenz zwischen den CCRs in Richtung des Beobachtungsvektors. Damit kann eine Ebene senkrecht zu diesem Vektor definiert werden die um die Entfernungsdifferenz verschoben ist. Der Schnittpunkt der Kugel mit der Ebene ergibt einen Kreis möglicher Positionen für den zweiten CCR. Sobald simultane SLR-Daten verfügbar sind, wird die kreisförmige Region durch den Schnittpunkt der beiden Kreise weiter auf zwei potenzielle Punkte im Raum verfeinert. Die beiden CCRs können nun mit einem Oberflächenvektor verbunden werden, der anschließend zur Rekonstruktion der Lage dieses Vektors über die Zeit verwendet werden kann. Diese Technik kann auch für eine größere Anzahl von CCRs verwendet werden, wenn deren wahre Anordnung bekannt ist und mindestens zwei CCRs identifiziert werden können.

Acknowledgements

Many people were involved to make this thesis possible. Therefore, I want to thank the Space Research Institute of the Austrian Academy of Sciences and their research group Satellite Laser Ranging. Special thanks belong to the group leader Michael Steindorfer and all other members of the group especially Peiyuan Wang, Franz Koidl and Daniel Fauland for their support during the time.

However, without the friends I made along the way during my time in Graz none of this would have been possible. I thereby want to thank everyone who supported me not only in my scientific career but also in my personal one. Special thanks to the whole Cake-Group and to the Scarf-Engineers.

My biggest appreciation though belongs to my caring family. I would like to express my deepest gratitude for your unconditional support during my time at the university.

Table of Contents

1	Introduction	1
1.1	Space Debris in General	2
1.2	Space Debris Removal	3
1.3	Attitude Estimation	6
1.3.1	Light Curves	7
1.3.2	LED-based	9
1.3.3	Image Sequence Interpretation / Radar Observations	9
2	Methods	11
2.1	Satellite Laser Ranging	11
2.1.1	Ground Segment: SLR-Station	13
2.1.2	Space Segment: Corner Cube Reflector	17
2.1.3	Differentiation of single CCRs	24
2.1.4	Bi-static Measurements	26
2.2	Attitude Estimation	28
2.2.1	SLR Residual Simulation Tool	28
2.2.2	CCR Placement for Differentiation	37
2.2.3	Calculation of Surface-Vector	40
2.2.4	Data Editing	49
3	Results and Discussion	55
3.1	Satellite Laser Ranging	55
3.1.1	Basic SLR-Simulation	55
3.1.2	Bi-static SLR Simulation	57
3.2	Attitude Conclusions based on single SLR-Station	60
3.2.1	Apparent Rotation depending on Elevation	60
3.2.2	Incident Angle	62
3.3	CCR Placement Differentiation	63
3.4	Surface-Vector	65
3.4.1	Surface-Vector over whole Pass	65
3.4.2	Data Editing	67
3.5	Attitude Estimation	70
3.5.1	Rotation Axis	71
3.5.2	Rotation Period	72
4	Conclusion and Outlook	75

List of Figures

2.1	Geographical locations of all GGOS stations	12
2.2	Basic structure of SLR	14
2.3	Velocity aberration	19
2.4	Theoretical Far-Field Diffraction Pattern	20
2.5	Spoiling	22
2.6	Radar Link Equation	23
2.7	Evidence of distinctness of single CCRs on the surface of a S/C.	25
2.8	Areas of possible distinction	26
2.9	Schematic of Bi-Static measurements	27
2.10	Terrestrial to Celestial Coordinate Transformation	32
2.11	Example CCR pattern	41
2.12	Example Simulation to Extract Residual Differences	42
2.13	Schematic to explain the incident angle	43
2.14	Principle of the cone approach	45
2.15	Cone idea with two SLR-Stations	46
2.16	Graphical result of the intersections of the two cones / spheres	47
2.17	Schematic cone idea on S/C	48
2.18	Example of a single chunk	50
3.1	Example SLR output file	56
3.2	Simultaneous observation simulation: Residuals	58
3.3	Simultaneous observation simulation: Azimuth and Elevation angle	59
3.4	Example of the impact of apparent rotation	61
3.5	Theoretical CCR placement	64
3.6	Theoretical CCR placement	65
3.7	Example pass for surface-vector	65
3.8	Example pass for surface-vector	66
3.9	Data separated in chunks	67
3.10	Separated example chunks	68
3.11	Iteration to combine sections	69
3.12	Iteration to combine sections	70
3.13	Schematic of Rotation Axis Estimation	71
3.14	Estimated vs. true rotation axis	72

List of Tables

2.1	Used values for evaluating the radar link equation.	23
2.2	Most important rotation parameters	30
3.1	Results of the apparent rotation variation	62
3.2	Results of the Incident Angle	63

Listings

2.1	Example file of the CCR input.	34
2.2	Main Output	38
2.3	Find NaN values	49
2.4	Find closest curve	52

List of Acronyms

CCD	Charge-Coupled Device
CCR	Corner Cube Reflector
CoM	Center of Mass
DORIS	Doppler Orbitography and Radiopositioning Integrated by Satellite
ESA	European Space Agency
FFDP	Far-Field Diffraction Pattern
FOV	Field of View
GCRF	Geocentric Celestial Reference Frame
GGOS	Global Geodetic Observing System
GNSS	Global Navigation Satellite System
ICRF	International Celestial Orbit Frame
ILRS	International Laser Ranging Service
ISAR	Inverse Synthetic Aperature Radar
ITRF	International Terrestrial Reference Frame
IVS	International VLBI Service
LED	Light Emmiting Diode
LEO	Low Earth Orbit
NORAD-ID	North American Aerospace Defense Command Identification
POD	Precise Orbit Determination
RCF	Reference Coordinate Frame
RLEq	Radar Link Equation
S/C	Spacecraft
sCMOS	scientific Complementary Metal–Oxide–Semiconductor
SLR	Satellite Laser Ranging
SoD	Seconds of Day
SPAD	Single Photon Avalanche Diode
TEME	True Equator Mean Equinox
TLE	Two-Line-Element
VLBI	Very Long Baseline Interferometry

1 Introduction

Not too many years ago before the first artificial satellite Sputnik 1 [Harvey, 1996] was launched in 1957, space was untouched by human kind. The only objects in Earth's orbit were of natural origin such as small pieces of cometary and asteroidal material like meteoroids or interplanetary dust [ASA, 2023]. Furthermore, the moon is part of Earth's orbit as a natural satellite in a broader sense. As a result of the Cold War and the ongoing "Space Race", the development of satellites was given a lot of attention. Soon after the Soviet Union managed to launch Sputnik 1, Sputnik 2 was also a success [Harvey, 1996]. After the first attempt failed to launch USA's first satellite Vanguard 1A in orbit, Explorer 1 was the first American satellite in space. It launched February 1st, 1958, only four months after the Soviets first successful orbiter [McLaughlin and Milton, 1970]. Satellites from other states followed in 1962, first by the UK with Ariel 1 [NASA, 1963] and then by Canada with Alouette 1, which is still in space [N2YO, 2016]. The first Austrian satellite, TUGSAT-1, was developed by the Graz University of Technology, the Vienna University of Technology and the University Vienna and launched in 2013. Following the initial successful attempts in launching various spacecraft (S/C) into orbit, the count of active satellites exhibited nearly linear growth until 2011 [Statista, 2024] with a light jump in numbers between 1996 and 1999. In 2011 the total number of satellites in orbit was just above 1000. Space exploration began its commercial journey in 1965 when AT&T launched Telstar, marking the start of the first commercial satellite in space [McLaughlin and Milton, 1970]. Initially, space operations were expensive. However, as technologies advanced, costs fell and reliability improved, paving the way for other companies to enter the space industry,

such as SpaceX. Subsequently, there was a shift to exponential growth, culminating in approximately 11,500 satellites in orbit by the early months of 2024, with around 9,000 of them still operational [ESA, 2024]. According to these numbers, 2,500 inactive S/C are still in orbit, either in the graveyard orbit or continuing uncontrolled on their original orbit, blocking it and jeopardising active satellites.

A graveyard orbit is a special type of orbit that can be used to position a satellite at the end of its operational lifespan in order to avoid any potential risks to active satellites. The energy required to reach the graveyard orbit is significantly less than what would be needed for a safe de-orbit. The graveyard orbit is situated just above the geostationary orbit with an altitude of about 36,050 km. Once in this orbit, the satellite can remain in a safe, high-altitude orbit for decades, without intersecting the geostationary orbit [Mejía-Kaiser et al., 2006].

1.1 Space Debris in General

With each new satellite launched into space, an increasing quantity of human-made material is brought into Earth's orbit, where it can ultimately become space debris. Space debris is any artificial object which is human-made, no longer in use or not functioning correctly and is in Earth's orbit. Such debris can range from the upper stage of a rocket to a defunct satellite, or even involve a lost toolbox belonging to an astronaut on the International Space Station. [NASA, 2023]. Due to the considerable high velocities, of approximately seven kilometers per second (depending on orbital height) [NASA, 2024], objects in space, including small particles resulting from disintegration, erosion, or collisions, pose a potential risk to both ongoing and upcoming space missions [ASA, 2023]. Understanding and managing this risk is vital to ensure the safety and success of any space operation.

In response to these challenges, collaborative efforts have started on the international stage. Initiatives like the European Space Agency's (ESA) Space Debris Office [ESA, 2024]

and the United Nations Office for Outer Space Affairs [UNOOSA, 2024] actively engage in monitoring, analysing, and the promoting the mitigation strategies for space debris. International agreements, such as the Space Debris Mitigation Guidelines established by the Inter-Agency Space Debris Coordination Committee, provide a framework for responsible space operations and debris mitigation practices [Mejía-Kaiser, 2020]. These organisations have to encourage all member states to completely mitigate every risk of the creation of new space debris. Additionally, space debris in low Earth orbit (LEO) leads to the so called Kessler Syndrome. This syndrome, proposed by NASA scientist Donald J. Kessler in 1978, describes a scenario in LEO where the density of space debris is high enough that collisions could initiate a cascading effect [Kessler and Cour-Palais, 1978]. Each collision generates additional space debris, further increasing the risk of subsequent collisions, creating a self-sustaining cycle of space debris proliferation. In 2009, he later proposed that models had already implied the instability of the space debris environment [Kessler, 2009]. Hence, it is crucial not only to minimize the production of new space debris but also to entirely prevent it. It is imperative that all states with space access engage in discourse surrounding the risks associated with the generation of new space debris. The ESA's objective is not only to prevent the creation of new space debris, but also to "*drive the development of technologies required for no more debris to be left in orbit by 2030*" [ESA, 2023]. This statement implies that ESA wants to remove space debris which is already in orbit as well.

1.2 Space Debris Removal

The removal of space debris may be achieved through the utilisation of both passive and active removal techniques. Passive methods rely on the application of natural forces or mechanisms to facilitate the gradual removal of space debris and its descent into Earth's atmosphere. The principal characteristic of passive debris removal is that it does not require any external artificial influence to be effective. When a satellite becomes inactive,

the passive debris removal precautions should be automatically initiated. The utilisation of passive space debris removal methods presents a number of advantages. They could be often more cost-effective than active techniques, as they require minimal technological interventions. Furthermore, these methods are inherently scalable, rendering them suitable for addressing even the smallest satellites, such as nano-satellites. Additionally, passive removal does not require any new satellite missions and therefore does not pose any risk for new space debris. However, passive debris removal does present certain challenges. It may take an extended period of time to clear the space environment, and the precision of these removal processes are not as high as with active methods [Thorpe, 2022].

The distinction between active and passive debris removal techniques lies in the application of forces. While active removal involves the deliberate application of a human-made external force, passive removal methods harnesses and exploits natural forces for the removal process, like Earth's magnetic field. There are lots of methods which can be considered active debris removal like collective, laser-based, ion beam shepherd-based, tether-based, satellite-based and other unconventional techniques [Priyant and Surekha, 2019].

- Collective: The Centre National D'études Spatiales (CNES) strategy is to do a ranking of space debris which has to be removed but does not actually operate debris removal. How to remove the ranked debris remains an open challenge. Non-technical challenges, autonomous spacecraft concepts, non-cooperative debris analysis, and prototype experiments have been underlined by recent studies, calling for more robust and validated solutions for effective removal of debris [Bonnal et al., 2013].
- Laser-based: Laser ablation is a well-studied process that has been researched for decades. An intense laser pulse is directed at the surface of a target, leading to the superheating and vaporization of a very thin surface layer. The hot material expands and is accelerated, exerting a force onto the target according to Newton's third law (actio est reactio). The laser debris removal method is a unique approach that utilises ground-based facilities to produce thrust forces, resulting in high removal

rates estimated to be in the range of hundreds of particles per day. While the method is currently limited to small particles and is purely theoretical at this stage, it aims to tackle the challenge of removing a significant number of small debris particles, thereby contributing to the mitigation of space debris in LEO [Phipps et al., 1988].

- Ion-beam shepherd-based: The method of the Ion-beam Shepherd is to project a beam of quasi-neutral plasma from a satellite onto space debris, which imparts some propulsive force to move and de-orbit it. Several researches were aimed at mass and thrust optimization of the shepherd satellite, stabilization of this satellite, plasma interactions, and solving technical problems connected with beam divergence, contamination and atmospheric effects [Bombardelli and Pelaez, 2011].
- Tether-based: This active debris removal concept based on tethers involves attaching a long wire to larger space debris. Due to the Earth’s magnetic field, it gets gradually de-orbited until it reaches the atmosphere and burn up. Various researches are focused on different approaches: electron collection, electrodynamic tethers in LEO and geostationary orbit, throw-nets and tow-tethers deployment, harpooning of debris, adaptive control strategies, flexible tethered-net systems, and hybrid tension control methods. Those enhance the feasibility and efficiency of tether-based removal of debris [Sanmartin et al., 1993].
- The final two methods, satellite-based and unconventional, will be considered together, as both involve the use of a satellite to capture the space debris or alter its orbit. However, there are currently no active missions but companies and facilities that are engaged in doing research in this area. The Swiss company ClearSpace is designing a mission where a chaser satellite should rendezvous, capture and de-orbit a defunct S/C [ClearSpace, 2024]. There is a number of approaches that have been developed to capture space debris. Using nets [Shan et al., 2019], harpoons [Tamaki and Tanaka, 2022], robotic arms [Mayorova et al., 2021] or a semi-fixed robot [Zhao et al., 2017]. Regardless of the concept at least two requirements

have to be met: One has to know where exactly the space debris is located, thus knowing the exact orbit. Additionally, knowing the attitude to a certain accuracy is crucial to avoid damaging intersecting satellites and generating additional space debris. Moreover, fragmentation should be minimized: During the capture of the defunct satellite, its structural integrity must be maintained. To accomplish this, the capturing satellite must synchronize with the rotation axis and period of the space debris [Liu et al., 2020]. However, estimating the attitude from ground would be beneficial. The capturing S/C could only estimate the attitude of the space debris while it is in close approach and would therefore need significantly more fuel to alter its attitude rapidly.

1.3 Attitude Estimation

The accurate determination of the attitude of space debris depends on the effective implementation of strategies and resources used. The ground-based methods used for the measurement of the attitude of space debris use a variety of technologies, each of which possesses both advantages and limitations. The majority of these methods are based on optical techniques, radar-based procedures or hybrid systems that use a mixture of data sources to enhance accuracy. One of the optical methods use the measurement of the strength of the solar radiation which is reflected by space debris [Schildknecht et al., 1997]. The rotation pattern and orientation can be determined by analysing the intensity variations of the reflected light. This technique permits straightforward data collection through the utilisation of ground-based telescopes and other optical sensors. However, this technique depends on good weather conditions and is restricted to the terminator period (station in the dark and space debris enlighten by the sun). Furthermore, it is less effective when the images are smaller or situated at greater distances. Radar-based techniques provide a complementary approach, including techniques such as an Inverse Synthetic Aperture Radar (ISAR). Such methods make use of Doppler shifts in radar signals

reflected from the debris in order to generate two-dimensional images. In particular, the ISAR technique uses the movement of the debris to create high-resolution images [Steele et al., 2005]. This technique enables the gathering of data on the structural characteristics and rotational dynamics of the debris, regardless of the lightening conditions. Nevertheless, this approach uses signal processing and is relatively resource intensive. Hybrid methods combine the benefits of optical and radar techniques by using the data from different sources to improve accuracy and reliability [Sánchez Piedra et al., 2023]. These systems can apply optical tracking for initial detection and approximate attitude estimation. In contrast the radar imaging methods are better suited to higher-detail analysis. In the majority of cases, higher-order algorithms and machine learning techniques are used to gain a higher understanding of the attitude of the debris, for example in the work of [Trummer, 2023] where light curves were analyzed. Each of these methods has a specific role to play within the broader context of space debris management. The continual advancement of technology is contributing to greater efficiency in their application [Deghuria et al., 2023]. The following sections will present these methods in detail, outlining the fundamental principles of their application and the latest developments in this field of science.

1.3.1 Light Curves

The method described in the paper "Optical Light Curve Observations to Determine Attitude States of Space Debris" by [Silha et al., 2015] for measuring light curves is carried out in the following steps: The light curves acquired at the Zimmerwald Observatory are obtained with the 1-metre ZIMLAT telescope, which is equipped with a charge-coupled device (CCD) camera and a scientific Complementary Metal–Oxide–Semiconductor (sCMOS) camera. These cameras offer particular advantages in terms of sampling frequency and automation. The telescope is capable of working in two distinct tracking modes: sidereal tracking, whereby it follows the stars in the background, and ephemeris tracking, which enables the predicted orbit of the space debris object to be monitored. Images are

captured with a CCD camera in a series of small sub-frame images, with an exposure time of only 0.2 seconds. The images are focused on the object in question, and the intensities are measured. The sCMOS camera is capable of imaging at a high sampling frequency of more than 10 Hz. The intensities are then subject to further processing in post processing. The light curves are constructed from a series of measurements of the intensity as a function of time. LEO objects are observed continuously throughout the duration of their pass, whereas higher orbit objects are observed in segments of up to 20 minutes. The intensity measurements may be converted into astronomical magnitudes using reference frames containing known stars. However, this step is not a requirement for the extraction of frequencies. The ZimSMART telescope uses the streak approach, where a single image is obtained over a long exposure time while tracking the stars. The intensity of the space object is measured along the length of the streak. This approach offers the advantage of high sampling rates with minimal use of telescope time. But there are certain limitations, including a relatively low signal-to-noise ratio for weak signal objects and less precise timing definitions.

This includes, but is not restricted to, Fast Fourier Transformation, Periodogram analysis, and Welch’s method [Solomon Jr. et al., 1991]. All these methods above require the light curve data to be linearly interpolated so that the final spacing of the data points becomes equidistant. Advanced techniques, such as the Lomb-Scargle periodogram [VanderPlas, 2018] or Epoch folding [Hakala et al., 2009], allow the actual unevenly spaced data points in most observation series to be analysed in a robust way. A second-order phase reconstruction is also made by dividing the light curve into segments according to the suspected period and comparing them in search of an optimum fit. Apparent spin rates and rotation characteristics, as derived by these methods, stand to be highly useful in remediation efforts of space debris, such as active removal and collision avoidance.

1.3.2 LED-based

[Marzioli et al., 2019] describes a method for attitude reconstruction and backup light communication using light-emitting diodes (LEDs) fitted on the external surfaces of the CubeSat LEDSAT for enhanced visibility and communication. During the process of attitude reconstruction, a variety of flash patterns are applied to the individual faces of the CubeSat. The patterns are primarily based on GPS PRN Gold codes, which ensure high auto-correlation values and low cross-correlation values, thus facilitating the recognition of patterns even from partially observed sequences. Subsequently, specific orientations are identified based on the manner in which the CubeSat illuminates its LEDs from ground-based telescopes. These flashing patterns are tested for suitability in various conditions, from variable tumbling rates through the addition of noise in a series of simulations. The observed pattern of LEDs is passed through a face recognition software against a pre-established library of known patterns to find a match that indicates the orientation. This involves averaging the luminous flux, correlating the observed sequences with stored patterns, even partially to determine the CubeSat's orientation. By doing so, the LEDs and their backup light source are utilized to transfer basic telemetry information. This technique is leveraging from the large emission angle of the LEDs. The system does not require point-to-point communication, instead using narrow filters to reduce background noise. It modulates the data onto the flashes of the LEDs, which the communication system receives using ground sensors such as CCD and CMOS cameras. Long exposure images record the dots and lines. Data encoded in this form can be decoded later to retrieve the information that was transmitted.

1.3.3 Image Sequence Interpretation / Radar Observations

The techniques used for the reconstruction of radar attitudes in the context of space debris are based on the temporal variations observed in radar cross-section measurements. They are capable of delivering the rotational states and specific orientations of space objects as explained in the work of [Zhou et al., 2019]. This manuscript presents a novel

approach based on the integration of target trajectory information and ISAR geometric projection models. In this method, shape features are extracted from ISAR sequences in order to estimate the attitude of the target and rectangular component sizes based on optimisation constrained by prior shape information. The method comprises three principal innovations:

- This approach goes beyond traditional matching to explicitly express the extracted features. Unlike traditional methods, it does not rely on existing databases in a routine manner. Instead, it enables the monitoring of non-cooperative space targets with partially known or unknown structures.
- The method takes into account the parameters of radar line-of-sight angles and ISAR image sequences together. Thereby enabling the interpretation of 3D attitude and geometry and the provision of precise vectors that reflect the absolute attitude of a target in Cartesian coordinates.
- The Radon transform is used in its original form to devise a parallelogram descriptor for the capture of rectangular components of a satellite target within a range-Doppler image frame. This significantly simplifies the association process, which is often complicated by the phenomenon of angular glint, and enables the automatic association of planar components such as solar wings in ISAR image sequences.

The superiority of the approach in terms of feature association and reconstruction feasibility is illustrated by comparative experiments. Furthermore, robustness analysis confirms the effectiveness of the algorithm in practical scenarios. The detailed implementation and experimental validation demonstrate the potential of the method for improving satellite target attitude estimation and geometry reconstruction using ISAR image sequences. Nevertheless, this approach is only viable when observing stable satellites. The dynamic estimation of a rotating space object is not feasible at this time, or at the very last, further research is required.

2 Methods

2.1 Satellite Laser Ranging

Satellite Laser Ranging (SLR) is one of four principle techniques to construct the Global Geodetic Observing System (GGOS). In addition to SLR, Doppler Orbitography and Radiopositioning Integrated by Satellite (DORIS), Global Navigation Satellite System (GNSS) and Very Long Baseline Interferometry (VLBI) are methods to realize the GGOS [Noll, 2008]. The services are represented by the International Laser Ranging Service (ILRS), the International DORIS Service, International GNSS Service and the International VLBI Service (IVS), respectively [Noll, 2008]. These facilities provide valuable data regarding the Terrestrial Reference Frame, the Celestial Reference Frame, Precise Orbit Determination (POD), Earth Orientation Parameters, atmosphere, gravity, timing and fundamental physics [Noll, 2008]. However, only SLR, GNSS and DORIS are capable of performing POD of satellites, and only SLR is able to observe space debris, as the other techniques would necessitate the use of active sensors or antennas on board to process the received data. In Fig. 2.1 the geographical locations of all stations are displayed. While SLR and VLBI stations are predominantly located in the northern hemisphere, GNSS and DORIS networks are global in scope. This is due to the fact that GNSS and DORIS systems are based on a single antenna, which is relatively inexpensive. Furthermore, the antenna requires minimal space and no active maintenance personnel. Both SLR and VLBI require an observatory to be equipped with a large telescope and a large antenna, respectively. In addition, trained employees are required to undertake the necessary mea-

surements and subsequent data processing. Consequently, the financial outlay required for such facilities is considerable, and a significant number of countries are unwilling to invest in this type of infrastructure [Noll, 2008].

In this work only SLR will be considered as it is the method with the most accurate results. SLR is based on the reflection of a ground emitted laser beam on the surface of a space object. The distance from the station to the space object can be calculated by the time needed for the laser beam to go back and forth to the space object and back to the station [Bartels et al., 2022]. Triangulated with other stations on the Earth the position and a prediction of the orbit can be calculated. It is important that for most S/C where a high precision orbit is required, one or more corner cube reflectors (CCRs)(see section 2.1.2) are mounted on the surface. Depending on the mounting position and return rate the single CCRs can be identified in the measurements.

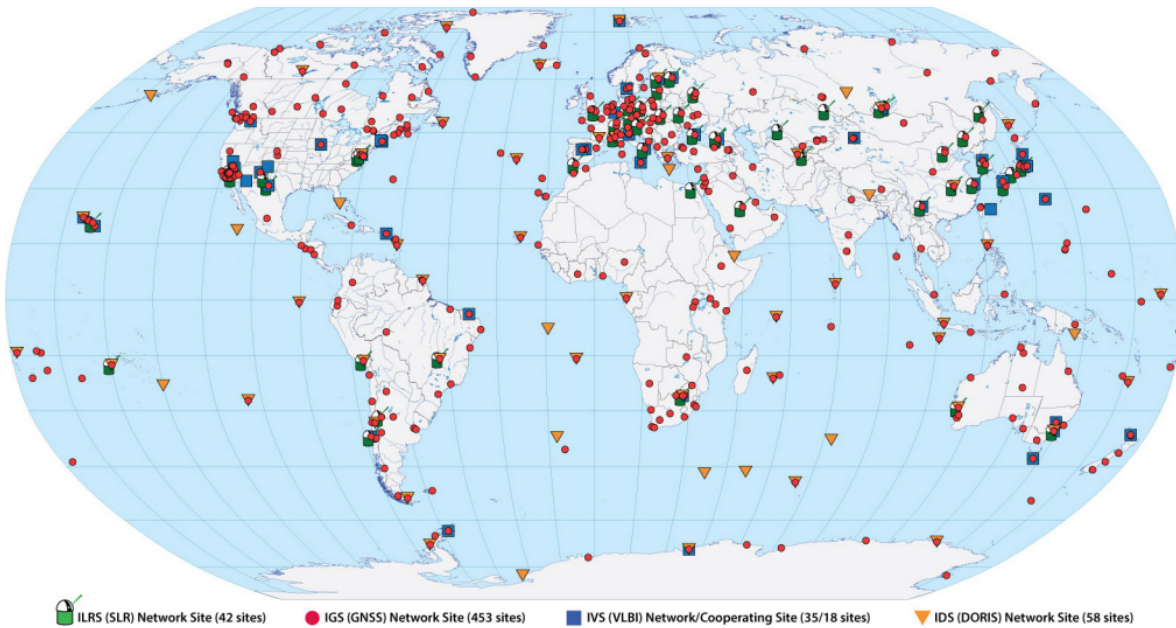


Figure 2.1: The geographical locations of all GGOS stations are indicated in the map above, which was created in 2014 [Noll, 2008].

2.1.1 Ground Segment: SLR-Station

By using the SLR method, the range between station and satellite can be calculated using a pulsed laser. To simplify, only the most important instruments needed will be explained in this section. This comprises a laser generator, a start/stop pulse detector, a clock, a mount, a receiving and a transmitting telescope. The basic structure is shown in Fig. 2.2. The laser generator generates in most cases a green (532 nm) or an infra-red (1064 nm) laser beam with a certain frequency. This frequency can vary from a few Hz up to MHz each having some advantages and disadvantages. Depending on the frequency each laser pulse can have a higher or lower energy. Higher frequency generally results in lower single shot energy and vice versa. The higher the energy of a pulse the more photons will be emitted in the same time. For example, a pulse with an energy of $400\text{ }\mu\text{J}$, will contain about 10^{16} photons. Once the laser has exited the generator, a start pulse is initiated that starts the clock. Subsequently, the laser is guided to the transmitting telescope, which is then aimed at the target. As a consequence of the divergence of the laser beam, only a proportion of the emitted photons will reach the target. The photons will ideally be reflected at a CCR or on the surface of the object. The receiving telescope is now able to capture the reflected photons, which are also thinned out due to divergence and diffuse reflection. Ultimately, only a few single photons will make their way back to the station, which will then trigger the Single Photon Avalanche Diode (SPAD). This will in turn trigger the stop pulse and halt the clock.

Laser

The latest generation of SLR systems which are currently operational, use high repetition rates, typically at 2 kHz. However, the use of MHz lasers is currently under development. These systems, including the solid-state Nd:YAG laser, are currently in use at SLR stations in Graz, Herstmonceux, and Changchun. These emit ultra-short pulses with a duration of around 10 ps and have an energy of around 0.4 mJ. In contrast, the traditional laser systems normally operate at a frequency of around 10 Hz and possess pulse

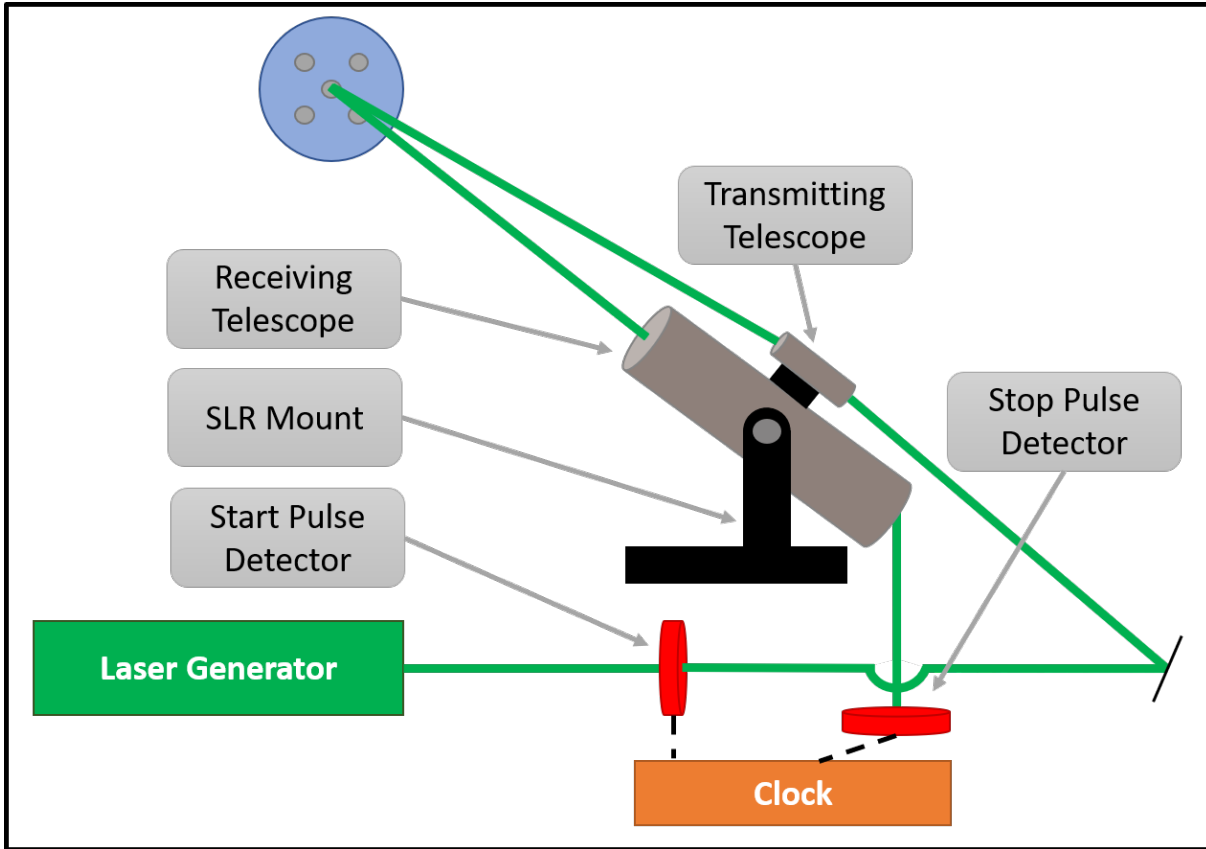


Figure 2.2: Basic structure of SLR.

energies ranging between 20 mJ and 100 mJ while having pulse widths that lie within the range of 50 ps and 100 ps. The narrower pulses mean high single-shot precision, and also a higher normal point precision because of the higher observation frequency. However, low signal-to-noise ratio calls for the application of sophisticated data processing techniques in order to differentiate satellite signals against the surrounding background noise. Real-time tracking software is used at the Herstmonceux station to evaluate normal point precision and allows satellite switching with prompt warnings once a precision of 1 mm is achieved. Systems that require a very high repetition rate must rely on an event timer, since the conventional interval timers cannot cope with the processing of overlapping range measurements. In order to get a fast update of the range gate window, systems using an FPGA board, which had been developed in Graz, have been realized. Another complication arising with kHz systems concerns laser fire overlap. This happens

when the detector is waiting for a returning pulse but is actually detecting backscatter from the following shot. This is mitigated by real-time adjustment to the laser fire rate, set between 1950 Hz and 2000 Hz. In conclusion the advances in high repetition rate SLR brought an increase in measurement accuracy and efficiency, however this entailed the development of more complex signal processing routines and some system adjustments [Tyagla, 2024].

Mounting and Telescope

The SLR ground station consists of different telescopes, mount control and cameras. The transmitting telescope has to guide and emit the laser pulses while the receiving telescope has to capture the few photons which are reflected at the target. Under special constructional conditions, it is also possible that the transmitting and receiving telescope are the same. The mount control has to steer the telescope in elevation and azimuth angle as accurate as possible, usually in the range of a few thousandth degree. In addition, the position and velocity of the station has to be known. To support the observation of satellites and space debris numerous cameras are installed to check the weather conditions or change the settings of the laser itself. The latter includes divergence or alignment with the telescope axis, by looking at the backscatter. During night-time a camera helps to roughly determine the time bias of satellites by centring them.

Detectors and Clock/Timer

The most used detector in the SLR community is the SPAD detector. SPADs are ultra-sensitive semiconductor devices, very fast in detecting single photons. The main principle behind the operation of SPADs is the avalanche multiplication. One single photon in a semiconductor material causes multiplication into a large number of electron-hole pairs. A typical process in the active area of the SPAD, with a single photon, is the creation of an electron-hole pair. This pair will then be subjected to high electric field, leading to avalanche multiplication of other charge carriers. The result is the generation of an

electric pulse that can be detected. The most significant aspect to realize with SPADs is their ability to detect single photons in Geiger mode, which biases the diode constantly above the breakdown voltage. This design allows an avalanche to be initiated by a single photon, giving rise to a PPP sensitivity that has been attributed to SPADs. Additionally, their time resolution is in the picosecond range, thus representing very good candidates for being applied in systems like high frequency laser pulse measurement. However, the SPAD technology also has two main drawbacks: The dark count and afterpulsing. Dark counts are spontaneous avalanches without any photon impulse resulting in false triggers. Afterpulsing means the act when secondary avalanches are following the initial event. It can most probably be assumed that additional research can solve these problems as well, further enhancing the sensitivity of SPADs and thus their application in high-precision fields [Buller and Collins, 2009].

The time-of-flight of the laser light to and returning from the satellite has to be measured with extreme accuracy, usually around 10 ps are required by SLR. Within 10 ps the laser already will have propagated 3 mm in space. Deriving accurate distance measurements requires this kind of precision. Further, the timer needs to be highly stable over both short and long term so that consistency in results is obtained. Traditional single shot interval timers have been in use in many SLR stations. Event timers, however, have become more favoured with the rise of kHz SLR systems, where there are multiple laser shots in flight simultaneously. Modern high-repetition-rate SLR systems require event timers to provide the necessary timing resolution and stability. They handle the additional complexity of multiple overlapping measurements. Thus, event timers are driven by this requirement for managing an increased data rate, extracting meaningful signals amidst potential noise, and overlapping returns [Kirchner et al., 2013].

2.1.2 Space Segment: Corner Cube Reflector

An optical device comprising three mutually perpendicular reflective surfaces, the CCR is capable of reflecting light or other electromagnetic waves back to their source, irrespective of the angle of incidence. This property renders the CCR useful in a multitude of applications, as evidenced by its deployment in SLR. The deployment of a number of CCRs on the satellites surface enhances the return rate of the incoming laser from the station. A CCR can be back-coated or uncoated and solid or hollow. The AI Back-Coated Solid CCRs have a reflectivity of about 0.78 and are commonly used on satellites in LEO. They are heavy and have a wide Far-Field Diffraction Pattern (FFDP), but absorb sunlight, causing thermal gradients. In contrast, Uncoated Solid (TIR-Total Inertial Reflection) CCRs have higher reflectivity, about 0.93, and polarization-induced effects. They have similar weight and far-field patterns to back-coated CCRs, but with reduced cross-section due to polarization. Hollow CCRs are rarely used, but have a high reflectivity (close to 1.0) and a narrow FFDP. Thermal effects can affect CCRs at the joints. The RIS sensor on the ADEOS satellite used a hollow CCR [Degnan, 2012][ILRS, 2024][eoPortal, 2012].

Peak Cross Section

The peak cross section of a CCR used in SLR is an indicator of how many photons of the laser beam will be reflected. The minimum cross section required for SLR to detect returns is estimated to be 10^4 m^2 [Georges III, 1998]. The peak cross section σ_{cc} of an unspoiled CCR with light entering perpendicular to the front surface is determined by the formula of [Degnan, 2012]:

$$\sigma_{cc} = \frac{\pi^3 \rho D^4}{4\lambda^2}. \quad (2.1)$$

where ρ is the reflectivity of the CCR, D is the CCR diameter, and λ is the wavelength of the laser. Therefore, the size of the CCR has high influence, with the power of four, on the peak cross section.

Velocity aberration

Velocity aberration is an effect that occurs in SLR when the reflected beam from a satellite is deflected in velocity direction from its expected position due to the relative velocity between the satellite and the ground station [Zhou and Sing, 2013]. It is caused due to the finite speed of light and is dependent on the relative velocity between the satellite and the ground station, as well as the orbital height and elevation angle of the satellite [Dmytryszyn et al., 2021]. Velocity aberration can cause notable signal reduction, particularly when larger diameter CCRs are used. Since the relative velocity v' depends on the orbital height and elevation angle a formula for the velocity aberration (α) can be written depending on v' [Degnan, 2012]. In the formula α is the velocity aberration angle by which the laser beam is deflected,

$$\alpha = \frac{2v'}{c}. \quad (2.2)$$

The following simple example is intended to illustrate this. Assume the SLR station is situated on the Earth's surface and a satellite is orbiting the Earth at a specific distance d . Fig. 2.3 shows that \mathbf{r} is the vector from the station to the CCR. To simplify the calculation, it is assumed that the CCR is directly at the zenith, therefore the length of the vector \mathbf{r} is the orbital height d . When the laser pulse is reflected by the CCR on the satellite, it returns to the SLR station at a different angle α due to the relative motion between the SLR station and the satellite. This effect is known as velocity aberration. When the S/C passes the zenith the S/C velocity v and the relative velocity v' are equal. Looking at the right side of Fig. 2.3, where a graph of the velocity aberration depending on orbital height and minimum and maximum elevation angle is shown. The red line shows the case where the elevation angle is 90° , therefore the S/C has to be in the zenith.

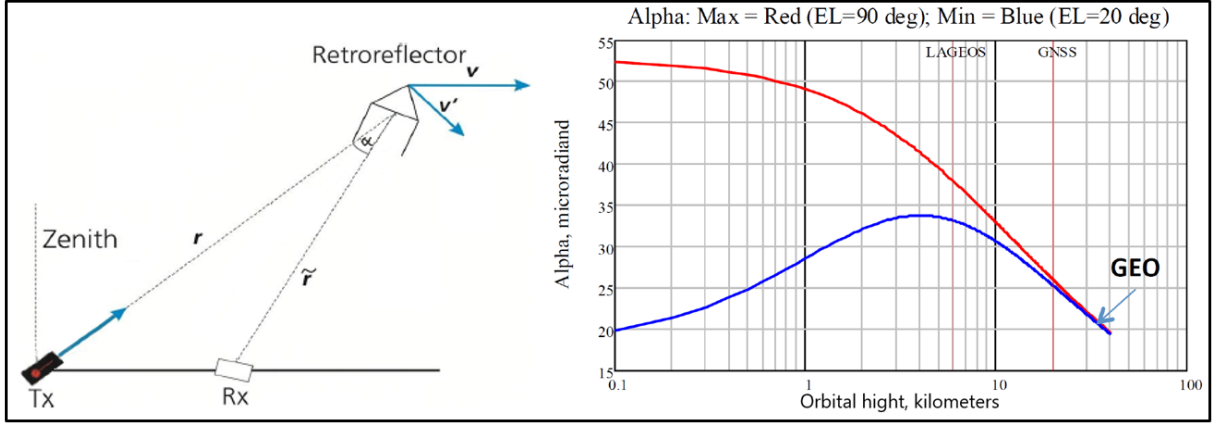


Figure 2.3: Velocity aberration; Left: Sketch of velocity aberration [Arnold, 2018]; Right: Velocity aberration (α Y-axis) depending on orbital height and elevation [Degnan, 2012].

Far Field Diffraction Pattern (FFDP)

The FFDP of a CCR is the pattern of the reflected laser beam as it spreads out from the reflector. It has a characteristic Airy-pattern with multiple lobes or peaks, which arise due to the interference of the light waves reflected from the three perpendicular reflecting surfaces of the CCR. The number and spacing of the lobes depend on the dihedral angles and dimensions of the CCR, and can be calculated using diffraction theory. With no dihedral angles applied, the main maxima contains the most energy of the laser pulse and with each side the energy maxima decreases. The total possible energy and the shape of the Airy-pattern is determined by the peak cross section which equals the size and reflectivity of the CCR. Additionally the velocity aberration determines at which position of the Airy-pattern the result will be. To understand the FFDP of a CCR Figure 2.4 summarizes important information. First of all, the cross section (black line) is normalized so that it is possible to extract the percentage of the maximum optical cross section than can be used under ideal circumstances. On the x-axis the parameter of the Bessel function 2.3 is illustrated. It depends on the off-axis angle theta (θ), the diameter of the CCR (D) and the wavelength (λ) of the laser. σ_{cc} is the peak cross section of the CCR and $J_1(x)$ the mentioned first Bessel function [Degnan, 2012],

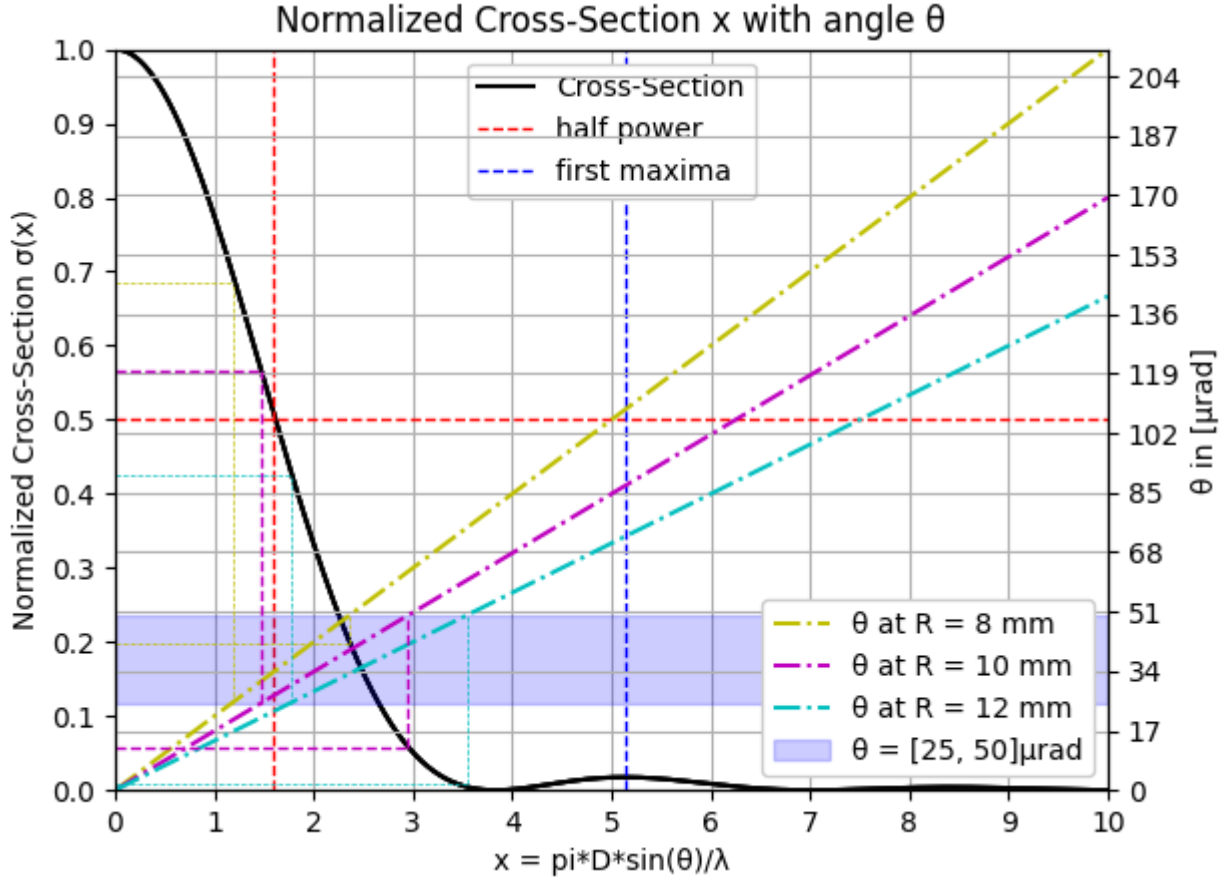


Figure 2.4: Theoretical FFDP for zero dihedral angles and LEO satellites with small CCR

$$\sigma(x) = \sigma_{cc} \left[\frac{2J_1(x)}{x} \right]^2, \quad (2.3)$$

$$x = \frac{\pi D}{\lambda} \sin(\theta).$$

The thick dashed lines show θ corresponding to a given CCR radius and constant wavelength, which directly compensates the velocity aberration. Therefore, the highlighted zone in light blue is the area of velocity aberration, which is important when talking about LEO satellites. A larger CCR has a narrower FFDP and is therefore better suitable for smaller elevation angles, corresponding in a lower velocity aberration, but has less intensity in higher elevation angles with larger velocity aberration. Conversely, a smaller CCR has better properties at higher elevation angles but an acceptable cross section in lower elevation angles.

Spoiling

CCRs have dihedral angles that are the angles between the three mirroring surfaces. These angles (β_{12} , β_{23} , β_{13}) are presented in Fig. 2.5 on the left side. The dihedral angle offset is the deviation from the perfect 90° angle. By changing the dihedral angles, the reflected laser beam can be broadened or narrowed in different directions, which can be used to compensate for velocity aberration [Atsushi and Sugimoto, 1994]. Broadening the beam will result in scattering the laser pulse energy over a larger area. This technique is called spoiling. When spoiling is used the angles generally will be changed by less than 2 arc seconds [Degnan, 1993]. The direction in which the beam should be broadened, narrowed or shifted can also be chosen by changing the dihedral angles of single surfaces [Stephenson, 2015]. If one or more of the dihedral angles deviate from 90° , the FFDP will change, causing the central lobe to split into a certain number of side lobes. The angular distance γ of the side lobes to the original center will increase with the dihedral angle offset according to equation 2.4 [Degnan, 2012]. There, n and δ represents the cube index of refraction the common dihedral angle, respectively,

$$\gamma = \frac{4}{3}\sqrt{6}n\delta. \quad (2.4)$$

A sketch of this effect is shown in the middle of Fig. 2.5. If the dihedral angle offset is the same for every plate, there will be a hexagonal symmetry of the lobes. The angular size of the lobe decreases with larger cube diameter and the peak cross section is reduced for each lobe [Degnan, 2012].

In Fig. 2.5 on the right side an example is shown where the CCR is designed to have the energy shifted in the second ring of the Airy-pattern. Moreover, the hexagonal shape is clearly visible.

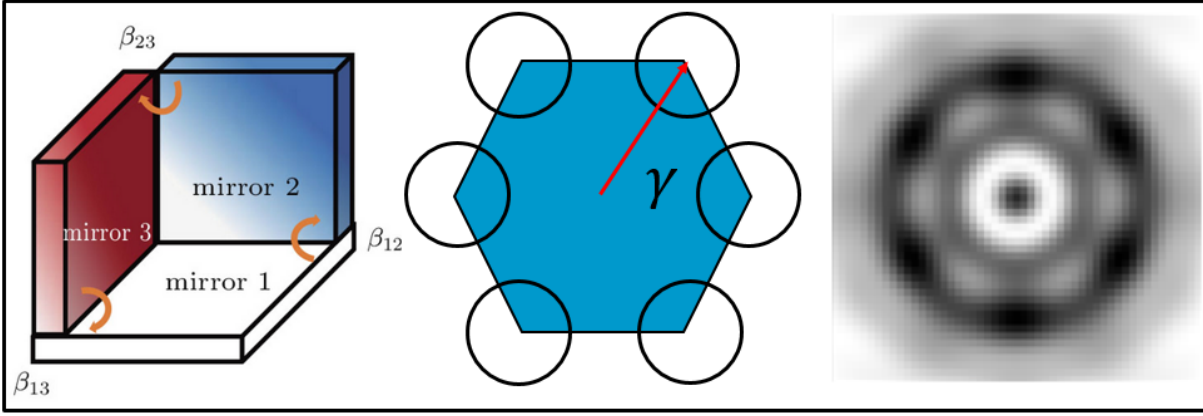


Figure 2.5: Spoiling; Left: Sketch of a CCR with dihedral angles [Yun et al., 2018]; Middle: Side lobes; Right: Energy shifted on second ring [Grunwaldt et al., 2016].

Radar link equation

The Radar link equation (RLEq) is often used to calculate how many photons the receiver can detect. Following [Degnan, 1993] used the expected return rate of CCRs can be calculated:

$$n_p = E_t \frac{\lambda}{hc} \eta_t \frac{G_t}{4\pi D^2} \frac{\sigma}{4\pi D^2} A_r \eta_r \eta_q T_a^2 T_c^2. \quad (2.5)$$

The explanation and typical values listed in Tab. 2.1. It is assumed, that the distance from the station to the satellite and the backward distance have the same length. In reality, due to the relative motion of station and satellite, the distances vary because of the light's finite velocity. Fig. 2.6 explains the number of photons which theoretically can be detected in dependence of the distance between station and satellite. The cross section is calculated for different CCR diameters using the values listed in Tab. 2.1.

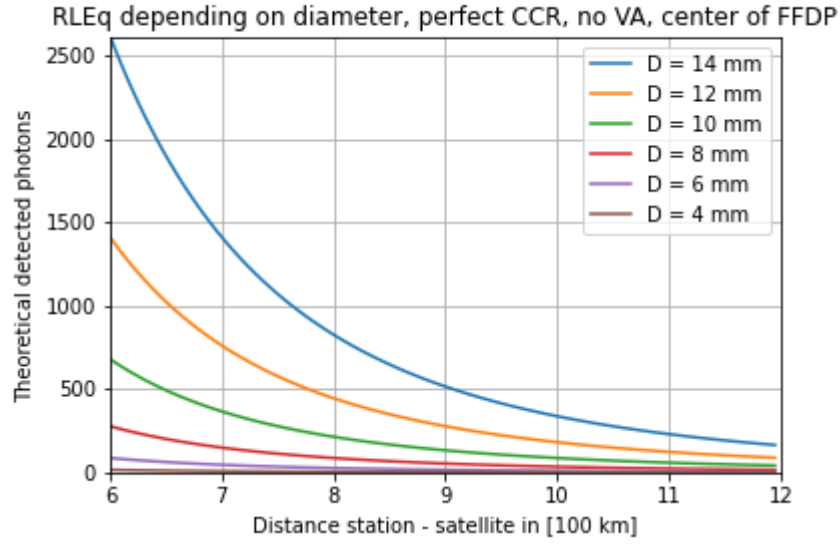


Figure 2.6: RLEq depending on diameter, perfect CCR, no velocity aberration, center of FFDP

Table 2.1: Used values for evaluating the radar link equation.

Var.	Typical Values	Explanation	Comment
n_p		Number of photons detected	The higher the better
E_t	$400 \mu\text{J}$	Laser source energy	One pulse at Graz-station
λ	532 nm	Wavelength of green laser	Some stations use 1064 nm
η_t	85%	Efficiency of transmitting optics	Estimation: 1% loss at each optical device
G_t	1.25×10^{10}	Transmitter gain	Estimation according to [Stephenson, 2015]
σ	$2.1 \times 10^5 \text{ m}^2$	peak cross section	E.g.: for diameter = 10 mm
A_r	0.196 m^2	Area of receiving optics	With telescope diameter 0.5 m
η_r	54%	Efficiency of receiving optics	Estimation: 3% loss at each optical device
η_q	20%	Efficiency of detector	Quantum Efficiency
T_a	0.65	Atmospheric transmittance	Visible range 10 km : According to [Jassmin and Kodeary, 2013]
T_c	0.8	Cirrus-clouds transmittance	According to [Degnan, 1993]

2.1.3 Differentiation of single CCRs

One of the key factors in estimating the attitude of space objects is the presence and positioning of CCRs on one or more surfaces. It is also essential to understand the specific arrangement of these CCRs. The ability to distinguish each CCR from the ground is crucial and ensuring the distinctiveness of the CCRs is therefore vital. This is important because the used method, described in section 2.2.3 use the mounting distance between each CCR for the calculation. However, to be able to take the right distance it is necessary to know which CCR is which. Fig. 2.7 demonstrates that, in practice, individual CCRs can be identified using SLR. This example examines the TechnoSat satellite (left panel), which features CCRs with varying patterns on each surface. The right side of the image shows the cleaned residual differences. As indicated, the A4 face with one CCR can be identified first, followed by the A3 face with four CCRs and then the A2 face with two. The residual line of the closest (lowest) CCR generates the highest number of returns. In case the SPAD becomes saturated after the first photons trigger the detector, not every valid photon from the other CCRs will be recognised. Consequently, the residual line of the closest CCR will always be the "thickest". In this example the the lowest/largest mounting distance between the CCRs are 30 cm and 140 cm, respectively. Even with shorter distance, it is possible to differentiate each residual line of each CCR. The dashed lines indicate the single CCRs. One of the issues that will require attention is the residuals of the A3 face. At the outset of the rotation, only three CCRs can be distinguished, but at the end, all four were visible.

The most crucial factor in determining distinguishability, is the mounting distance on the surface, which represents the maximum possible distance in the residuals. It should be emphasized that SLR is only measuring the range difference between the individual CCRs in the observation vector direction. If the surface of the S/C would be perpendicular to the observation vector, the residual distance between two CCRs would be zero, allowing no differentiation at all. Therefore, regardless of the distance between the CCRs, there will always be some attitude states where distinction is not possible. However, in general

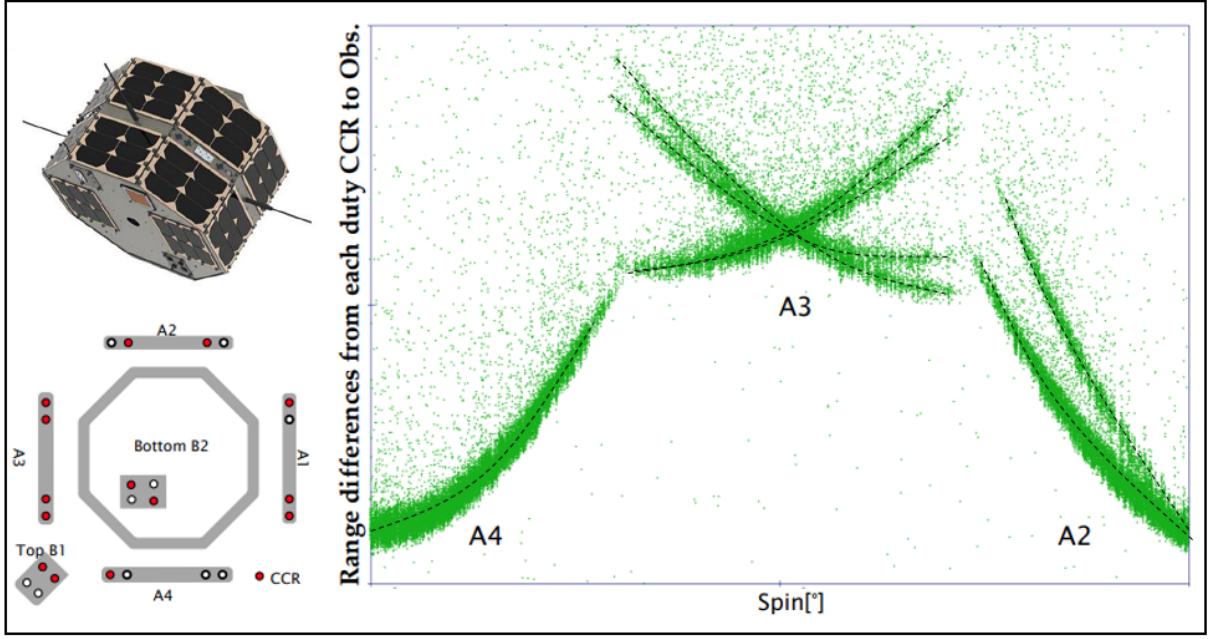


Figure 2.7: Evidence of distinctness of single CCRs on the surface of a S/C. Upper left: Picture of TechnoSat [Kramer, 2014]; Lower left: CCR pattern on each surface [Wang, 2018]; Right: Measured residuals from SLR-Station Graz [Wang, 2018].

it is sufficient to distinguish each CCR once per revolution per face, as conclusions can be drawn for the rest of the pass concerning the residual lines.

The accuracy of SLR measurements vary from station to station and are always depending on weather conditions. Nevertheless, almost all stations have an accuracy better than one centimeter. In Fig. 2.8 the possibility to distinct two CCRs which are placed 30 cm apart with an SLR accuracy of one centimeter is shown. On the left side the green color shows the area where distinction is possible depending on the incident angle and the rotation of the surface. On the right side the residual span (residual distance) depending on the incident angle and the rotation of the surface is shown. The two CCRs are not distinctable if the residual distance is lower than one centimeter. This happens either when the observation gets close to perpendicular to the surface (incident angle is zero) or an imaginary line which connects the two CCRs becomes perpendicular to the observation vector. The first case can be found on the far left of both schematics where

the residual span becomes zero. The second case happens two times in this example: At 0° and 180° surface rotation. Nevertheless, in almost 80 % of all cases a separation is possible. Since it is sufficient to separate the CCR once per revolution, it is save to say that a separation of the CCRs is possible for most passes.

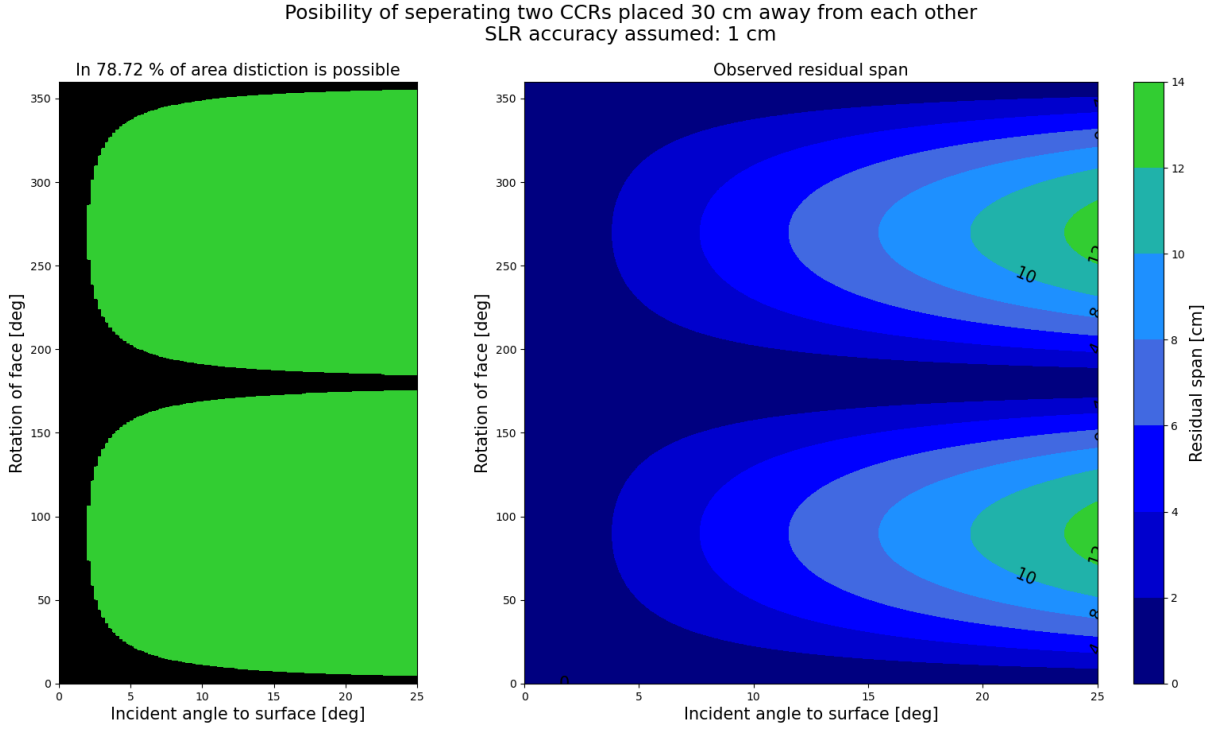


Figure 2.8: Areas of possible distinctions. Left: Possibility of distinction depending on incident angle and rotation of surface. In the green area distinction is possible. Right: Residual Span depending on incident angle and rotation of surface.

2.1.4 Bi-static Measurements

The idea behind bi-static measurements is to observe space objects with CCRs mounted on at least on face, from two different SLR-stations at the same time. Fig. 2.9 illustrates the general principle. Station A (*blue*), and station B (*red*) are observing the surface of a S/C with two CCRs on it simultaneously. The residuals for stations A and B are r_1, r_2 and r_1, r_2 , respectively. Note that the observation vectors, O_A and O_B , are assumed to be parallel to each CCR, respectively. That means that O_A has the same incident angle

when hitting CCR_1 and CCR_2 . Same behavior is true for the the observation vector of Station B. This assumption can be made because the satellite targets are several hundred kilometres away from the SLR station, while the two CCRs are at most a few metres apart. Therefore, the resulting difference in the angle is neglectable.

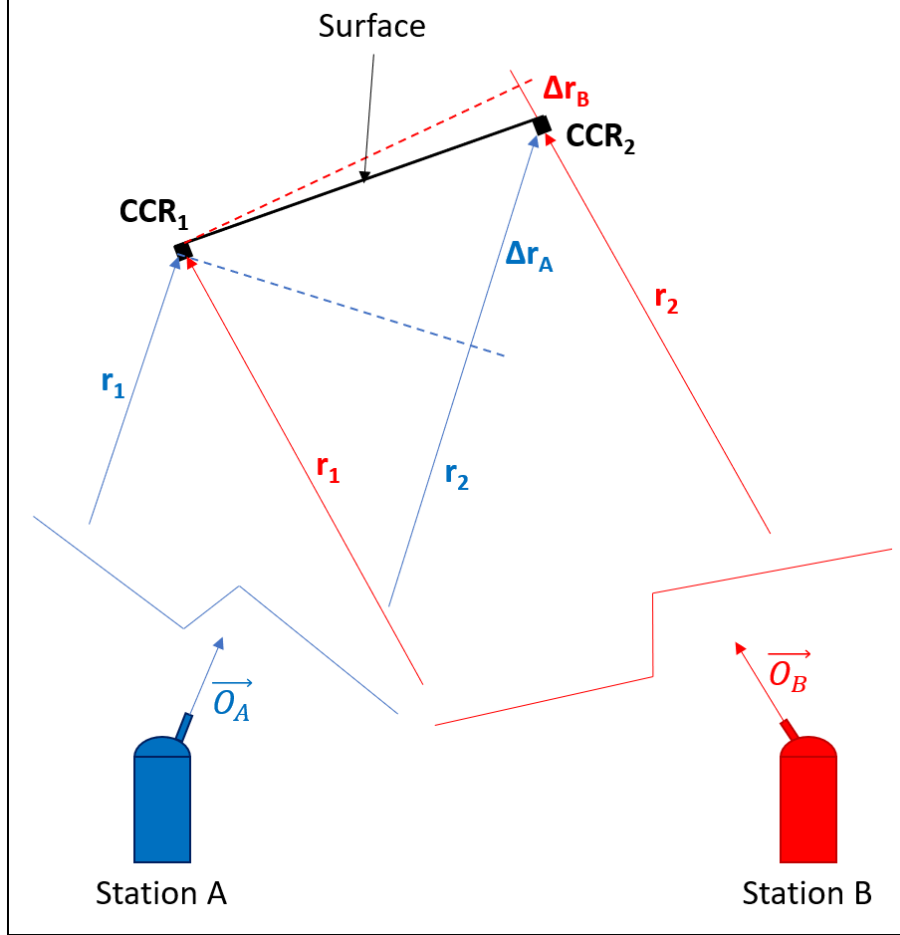


Figure 2.9: Schematic of Bi-Static measurements.

An important value is the range difference between the two CCRs, Δr , for each station, as this number is later needed in the calculations. It can be calculated using the equation 2.6, where r_1 and r_2 are the distances from the SLR-station to CCR_1 and CCR_2 , respectively. The difference in the range is called residual difference, Δr .

$$\Delta r = |r_1 - r_2| \quad (2.6)$$

By analysing the residual differences between the two measurements, it is possible to draw conclusions about the attitude. The given figure presents a simplified representation of the problem in two dimensions, which provides an insight into the underlying concept. However, in reality, the problem is three-dimensional, with the surface and the CCRs able to rotate.

2.2 Attitude Estimation

In this section the established SLR residual simulation tool is introduced and the possibility how to make attitude conclusions is described. Furthermore, the ideal CCR placement, the calculation of the surface-vector and which data editing steps are necessary will be discussed.

2.2.1 SLR Residual Simulation Tool

The SLR residual simulation is based on the Master's thesis of [Hofwimmer, 2021]. For the purposes of this work, the program was adapted, modified, and supplemented to achieve the desired performance, adaptability and functions. Despite the significant alterations, the fundamental structure of the program remains similar.

Read Input File

To start the simulation one of the most important steps is to define an input file. A file format which is readable by computer programs and humans is chosen: JavaScript Object Notation (.json). For each different simulation this file has to be defined and filled with the desired values. It consists of seven parts: Spacetrack, Station, ID, Pass, Rotation, Laser Retroreflector Array (LRA), and Field of View. The input has to be defined before the simulation, however, within the simulation class certain parameters can be changed without loading a new input file. Following, the most important input parameters within the parts will be discussed.

- **Spacetrack**

In this section the credentials, username and password, for the Spacetrack homepage (www.space-track.org) are stored in order to automatically download the Two-Line-Element (TLE) files of the used satellites. Spacetrack is a free homepage developed by SAIC where everyone can create an account and download the TLE files of a very large database of satellites and space debris objects.

- **Station**

In the Station section the Monument number of the station is saved. This number is given by the ILRS to identify each station worldwide and can be found at the ILRS homepage [ILRS, 2024]. This is necessary because in the simulations, passes over specific SLR-stations can be investigated and therefore the position and velocity of that station is needed. By providing the station number a sinex file is downloaded which contains the exact location of the station at the current time.

- **ID**

The ID defines the satellite whose orbit will be used for the simulation. Based on, the name and the North American Aerospace Defence Command Identification Number (NORAD-ID) the satellite is uniquely defined and in combination with the pass time the corresponding TLE file can be downloaded.

- **Pass**

In this part, the time of the pass has to be defined. If a TLE file is used the start and at the end epoch of the pass has to be known, the information is mandatory in order to perform the simulation. Otherwise it would be possible that the program simulates a not realistic scenario, where the station actually is not able to range to the target (below the horizon). Furthermore, the resolution of the simulation has to be defined (default 1 second).

- **Rotation**

Here, the rotation parameters and coordinate frame can be defined. In Tab. 2.2 the most important inputs are listed and shortly described. According to the project the rotation axis is assumed to be constant with respect to an inertial system. At the start of the simulation the rotation axis is defined in the body fixed system. During the simulation the body fixed axes will change but the rotation axis remains constant with respect to an inertial reference system (e.g. Geocentric Celestial Reference Frame (GCRF)).

The reason for the definition of the rotation axis in the body-fixed system is, on the one hand, that independently of the chosen reference system the rotation axis is always defined in the same system and on the other hand that one can imagine the possible rotation better. A possible rotation is easier to imagine in the body-fixed system than in the GCRF. The goal is to generate simulated residuals that can be used to test the attitude reconstruction.

Table 2.2: Most important rotation parameters

Parameter	Input	Description	Example
Include Rotation	boolean	The rotation can be either activated or deactivated	true
Rotation type	string	The rotation type can be chosen	const_vec
Reference frame	string	The reference frame can be chosen	gcrf
Rotation axis frame	string	The frame in which the rotation axis is defined can be chosen	body fixed
Rotation axis	array (1x3)	The rotation axis (XYZ) initially defined in body fixed system at $t = t_0$	[0.5, 0.5, 1]
Interval rotation steps	float	The time interval for simulation	1
Rotation angle	float	The degree for a full rotation can be defined	360
Initial rotation x/y/z	float	The initial angles at the beginning of the simulation	0
Rotation period	float	The duration of one full rotation is seconds	170

- **LRA**

The LRA (laser ranging array) section contains the location of the positioning file of the CCRs, which itself induces the position, normal vectors and eventually the FOV (half cone) of each CCR. Furthermore, it contains a color code for each face of the satellite so that the CCR can be later distinguished in the plots. Optional: the FOV selection for each CCR.

- **FOV**

If the FOV was not chosen separately for every CCR the default value for the FOV is given in this section. This value defines the acceptance angle (half cone).

Predictions

As stated in the previous part, a TLE file will be downloaded based on the NORAD-ID and the pass time. However, before a new file will be downloaded from Spacetrack, it will be checked if an appropriate file is already in the TLE-file folder to avoid unnecessary server traffic. This does not only save time, it is also required by the service provider. All TLE files will be saved in the same folder to be able to check their presence. Once a TLE file has been read in, the orbit of the specified satellite is calculated. To accomplish this task, the method of [Vallado, 2016] is used, which creates the data points in the True Equator Mean Equinox (TEME) coordinate system [Tieber-Hubmann, 2024]. The python library, which is released from Vallado's webpage is called *sgp4*. After that the data points have to be converted to ITRF and GCRF for further calculations. The steps in which the data transformation is happening listed in Fig. 2.10. For the simulation, TLE files were used because they can easily be downloaded and the only other input needed is the time interval of the pass over a specific station. In order to simulate the residuals and the attitude of a s/c the orbit does not need to be known as precise as for Earth observing satellites. Therefore, the orbit provided by TLE files is sufficient.

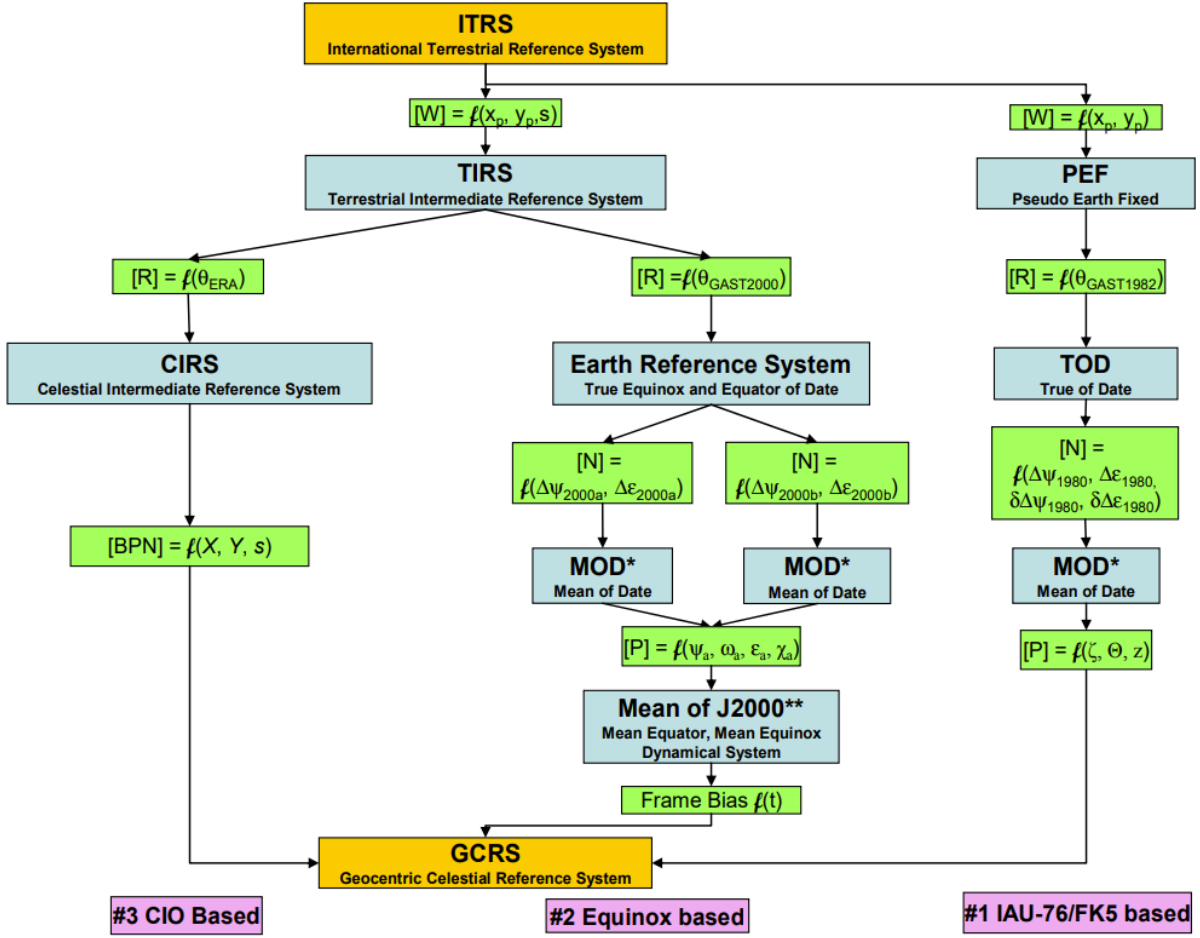


Figure 2.10: Terrestrial to Celestial Coordinate Transformation [Vallado, 2016].

Stations coordinates

Based on a sinex file (.snx) the current XYZ position of a SLR-station is gathered. The data is provided by the Crustal Dynamics Data Information System [CDDIS, 2024]. It is mandatory to have precise knowledge of the locations of all stations of which the data is being used to know when a s/c will become visible and to get the correct observation vector. The stations coordinates will be saved into ITRF format and might need to be transformed into the GCRF if the observation vector is given in GCRF as well.

Coordinate transformation

It is unavoidable within the SLR-Residual tool that coordinate transformations will need to be carried out on numerous occasions. The predictions of the pass as well as the coordinates of the SLR-station must be transformed to GCRF, because they are given in the ITRF. However, some unit vectors need to be defined in the ITRF to describe the orbital movement more easily. The Rotation axis must to be transformed in the GCRF, if not already defined in this coordinate system.

There are some reference systems which can be used when describing the motion of space objects. The ITRF is a geocentric system, with the centre of origin situated at the CoM of the Earth. Furthermore this frame is a non-inertial rotating coordinate frame, which results in the unit vectors that are building the orthogonal base are able to change and accelerate over time. The XZ-plane contains the Greenwich meridian, where the z-axis points towards the north pole. The y-axis is set up accordingly (right hand rule) perpendicular to both the x- and z-axis [BEV, 2024]. Hence, the unit vectors and center of origin is constantly changing when observed from a point far in the vast universe.

An alternative option is the GCRF, a system with its centre of origin at the Earth's CoM. In contrary to the ITRF system the GCRF system is a inertial system which means that the orientation of the unit vectors do not change over time. For an observer situated at a vast distance, the reference axes remain fixed. The GCRF uses reference stars to define the orthogonal base. The reference stars or quasars are measured by VLBI maintained by the IVS [Vallado, 2016].

In this work TLE are used to calculate and simulate the orbits. They are published by the United States Space Command via SpaceTrack and Celestrak [Vallado et al., 2006]. They contain the Kepler elements to rebuild the orbit like epoch, inclination, right ascension of ascending node, eccentricity, argument of perigee, mean anomaly and mean motion as well as the first and second derivative [Khairallah, 2021]. TLE require simplified perturbation models (SGP) because TLEs offer a simplified set of orbital parameters that do not account for all forces acting on a satellite. SGP models correct for factors such as

Earth's non-uniform gravity, atmospheric drag and other perturbative forces caused by solar radiation or lunar gravity. These models are essential for calculating the position and velocity of a satellite with great precision, taking into account the effects of these influences over time and across different orbits. Without SGP models, the TLE data alone would not be enough to calculate precise orbital states [Vallado and Cefola, 2012].

Lagrange interpolation of specific pass

With the help of the Lagrange interpolation it is possible to interpolate the XYZ pass in a given interval. This method saves computation time for the transformation of the TLE file to TEME and GCRF.

CCR information

The positioning file of the CCR is saved in a separate file which location is stated in the input JSON file. In this file the most important CCR parameters used in the simulation are stored and shown below:

Listing 2.1: Example file of the CCR input.

1	A1-1	+0.7500	-0.7000	+0.7000	+1	+0	+0	b	45
2	A1-2	+0.7500	-0.7000	-0.7000	+1	+0	+0	b	45
3	A1-3	+0.7500	+0.7000	+0.7000	+1	+0	+0	b	45
4	A1-4	+0.7500	+0.7000	-0.5000	+1	+0	+0	b	45
5	A2-1	+0.7000	+0.7500	-0.7000	+0	+1	+0	g	20
6	A2-2	-0.0000	+0.7500	-0.7000	+0	+1	+0	g	20
7	A2-3	-0.7000	+0.7500	+0.0000	+0	+1	+0	g	20
8	A3-1	-0.7500	+0.3000	-0.3000	-1	+0	+0	r	45
9	A3-2	-0.7500	-0.3000	+0.3000	-1	+0	+0	r	45
10	A4-1	+0.0000	-0.7500	+0.0000	+0	-1	+0	m	30
11	B2-1	+0.7000	+0.3000	-0.7500	+0	+0	-1	k	15
12	B2-2	+0.3000	+0.7000	-0.7500	+0	+0	-1	k	15
13	B2-3	-0.7000	-0.3000	-0.7500	+0	+0	-1	k	15
14	B2-4	-0.3000	-0.7000	-0.7500	+0	+0	-1	k	15

The second column shows the name of the CCR, in this case the name was chosen depending on which face the CCR is mounted. A2-3 for example is the third CCR on the A2 face. The name of the CCR is not important for the simulation, but if changes happen

to the positioning the location of the exact CCR is easier found. The next three columns describe the XYZ position if the CCR with respect to the CoM, with the unit meter. The coordinates given are defined in the body fixed reference frame, which means no matter how the S/C rotates those vectors stay the same. The same applies for the normal vector of those CCRs which can be found in the next three columns. After that, the color of the CCR is defined to be able to separate them in the plots afterwards. The last column is not mandatory and states the FOV (half cone) of each CCR. If no value is given the FOV will be set to the default FOV given in the input file.

Rotate CCRs and body axis

In this step the CCRs which are defined in the body frame rotated along a defined rotation axis. Initially the body axes are assumed to be aligned to the reference coordinate frame (RCF) coordinate axis (but just for $t = t_0$):

$$e_x = \begin{bmatrix} 1 \\ 0 \\ 0 \end{bmatrix}, \quad e_y = \begin{bmatrix} 0 \\ 1 \\ 0 \end{bmatrix}, \quad e_z = \begin{bmatrix} 0 \\ 0 \\ 1 \end{bmatrix}. \quad (2.7)$$

First, the body (including body axes, retroreflector positions and rotation axis) is rotated around the three body axes by all three angles to an initial position. This then leads to the body axes and the rotational axis to be oriented somewhere with respect to the RCF (and not aligned to e_x, e_y, e_z any more). After that, the body is rotated accordingly around the rotation axis to define the position of the CCRs along time. In the JSON file a RCF can be chosen, e.g., GCRF, LOF or body fixed. The XYZ positions will be added to the selected RCF axis, which can look like the following equation 2.8 where the RCF is selected to be GCRF,

$$xyz_{rot_{itrf}} = x_{0_{itrf}} + e_{x_{grf}} * x_{body} + y_{0_{itrf}} + e_{y_{grf}} * y_{body} + z_{0_{itrf}} + e_{z_{grf}} * z_{body}. \quad (2.8)$$

However, to calculate the the final residuals of each CCR, the difference to CoM has to be calculated. In equation 2.9 the difference between the length of the vectors to the CoM and to the single CCR from the ground station is calculated and therefore, the final residuals, r ,

$$r = |\overrightarrow{CoM}| - |\overrightarrow{CCR}|. \quad (2.9)$$

Note that the goal of the simulation is to find methods for estimating the attitude behaviour of a constantly and linear rotating S/C or space debris. Therefore, not the free-tumbling case is simulated but the residuals which are generated due to a fixed rotation axis with respect to an inertial reference frame. However, it can be assumed that a constant rotation axis (with respect to the inertial frame) is a good approximation for most cases of a single pass. To estimate the possibility of the attitude reconstruction, the exact physical motion (free-tumbling) is not necessary. In fact, the baselines and the patterns of the residuals are more important.

Plot and save results

The results are saved in six different files. Three files contain the orientation of the X, Y and Z axis along the orbit over time (in terms of quaternions). Another file contains a detailed header with the most important information of the used parameters, as well as the residuals of each CCR. Those first four files are all text-files that contain useful information in order to calculate the attitude.

The next output is a single page divided in four main parts. Firstly, a short text part that contains that contains settings used in the simulation. Secondly, a graphical output showing the S/C and its CCRs with the corresponding normal vectors as well as the rotation axis. Thirdly, the residual plots, where each CCR is marked with their own color, over time. Lastly, the elevation and angle between observation vector and rotation axis over time. The last file is the JSON file used for the definition of the input.

The following script 2.2 shows and explains an example of the main output. The file contains all the data required for subsequent calculations and for the simulation to be reproducible.

In the first line the name of the satellite and the NORAD-ID is displayed. In lines 3 to 5 the data source and the time step is given. A smaller time step will result in a more accurate simulation, but will also require a longer calculation time. In the next block (lines 7 to 11) the rotation type and the rotation parameters are stated as well as the reference frame it is defined in. The next block (lines 13 to 16) contains the TLE file as a whole and then the start end end time of the pass (lines 18 to 21). After that, the whole CCR position and orientation information is given together with the standard FOV of the CCRs if no individual FOV is stated in the input file. The last block (line 43 onward) comprises the main information: namely the residuals of each CCR over time. The value "nan" means, that the CCR is not visible to the station, therefore the station is outside of the FOV of the CCR. Note that this file is much longer than shown here, but for better readability the residual section was shorten, significantly.

2.2.2 CCR Placement for Differentiation

For further calculations and estimations, it is mandatory to know which residual lines in the measurements belong to which CCR. For geometry reasons it is not possible to use a symmetric pattern like a rectangular, square or any other geometry which has ambiguities depending on the observation angle. This would lead to more than one possible assignment of the CCRs. Therefore, a pattern is needed where the distance between each single CCR is unique and the deviations are big enough so it can be measured by SLR. To ensure that the deviation gets as big as possible, the product of the squared distance differences is maximized, following

$$\max \left(\prod_{i,j} (|d_i - d_j|)^p \right), \quad \forall i \neq j, \quad \forall d \mid d \leq \sqrt{a^2 + b^2}. \quad (2.10)$$

Listing 2.2: Main Output

```

1      TECHNOSAT: 42829
2      -----
3      Settings:
4      Data source: tle
5      dt_pass = 1
6      -----
7      Rotation type: const_vec, body fixed rotation axis [x, y, z]:
8      0.707 0.707 0.0
9      reference frame: gcrs
10     Rotation periode in[s]:
11     80
12     -----
13     TLE-File:
14     TECHNOSAT
15     42829U 17042E   22031.57405207   .00001073   00000-0
16     11216-3 0   9992
17     42829  97.4380 253.5727 0015585 103.5673 256.7283
18     14.91500985247680
19     -----
20     Start time:
21     2022-01-31 19:05:00
22     End time:
23     2022-01-31 19:18:00
24     -----
25     CCR position and orientation info:
26     Name, x, y, z, normal x, normal y, normal z,
27     plot color, FOV (if given: half cone [deg])
28     A1-RA1 0.75 -0.7 0.7 1 0 0 b
29     A1-RA2 0.75 -0.7 -0.7 1 0 0 b
30     A1-RA3 0.75 0.7 0.7 1 0 0 b
31     A1-RA4 0.75 0.7 -0.5 1 0 0 b
32     A2-RA1 0.7 0.75 -0.7 0 1 0 g
33     A2-RA2 -0.0 0.75 -0.7 0 1 0 g
34     A2-RA3 -0.7 0.75 0.0 0 1 0 g
35     A3-RA1 -0.75 0.3 -0.3 -1 0 0 r
36     A3-RA2 -0.75 -0.3 0.3 -1 0 0 r
37     A4-RA1 0.0 -0.75 0.0 0 -1 0 m
38     B2-RB1 0.7 0.3 -0.75 0 0 -1 k
39     B2-RB2 0.3 0.7 -0.75 0 0 -1 k
40     B2-RB3 -0.7 -0.3 -0.75 0 0 -1 k
41     B2-RB4 -0.3 -0.7 -0.75 0 0 -1 k
42     -----
43     Standard FOV in deg:
44     18.75
45     -----
46     Time step, CCR 1, CCR 2, CCR 3, CCR 4, CCR 5, CCR 6, CCR 7,
47     CCR 8, CCR 9, CCR 10, CCR 11, CCR 12, CCR 13, CCR 14
48     68821.0, nan, nan, nan, nan, nan, nan, nan, nan, nan, nan, nan, nan, nan
49     68822.0, nan, nan, nan, nan, nan, nan, nan, nan, nan, nan, nan, nan, nan
50     68823.0, nan, nan, nan, nan, nan, nan, nan, nan, 0.6026371703483164,
51     0.8245727918110788, nan, nan, nan, nan, nan
52     68824.0, nan, nan, nan, nan, nan, nan, nan, nan, 0.6162031064741313,
53     0.8211661824025214, nan, nan, nan, nan, nan
54     68825.0, nan, nan, nan, nan, nan, nan, nan, nan, 0.6293669329024851,
55     0.8174370881170034, nan, nan, nan, nan, nan
56     68826.0, nan, nan, nan, nan, nan, nan, nan, nan, 0.6421133223921061,
57     0.8133885553106666, nan, nan, nan, nan, nan

```

In this equation 2.10, d is the difference between the distances from one point to another. The power p can be varied to change the quickness of the falling approximations. If there were three CCRs on the surface, the product would be: $(d_1 - d_2)^2 * (d_2 - d_3)^2 * (d_3 - d_1)^2$. This method excludes the cases where two CCRs would have the exact same distance to another, because Δd would be zero, thus the product would also be zero. If they would be too close to each other Δd would become very small, because the two CCR would have a similar distance to the third one. To ensure that one distance will not exceed the rectangular surface, d is not allowed to get larger than a diagonal (last part of the equation).

To solve this problem a function in Python was implemented, which finds the most promising CCR positions using numerical approximation. The steps to archive the perfect CCR pattern are described in following list.

1. Definition of input parameters

Rectangular surface area: describes the size of the possible positions where the CCRs can be placed. The input are two lists. Within a list described the start and end position in the x- and y-axis are described.

Number of CCRs: In this thesis the focus was on the placement of three because a specific pattern was found where basic distinction is possible.

Grid-size: The more grid points there are, the longer the calculation will take, but the results are more accurate. The input is a list with points in x and y direction.

Initial points: Two initial points are by default in the corners of the surface, since this is the largest distance possible, but can be changed if needed.

Power: The power of the difference in the product to ensure sharper edges in the solution (default value: 2).

2. Creation of the grid

A grid which covers the whole surface with the given number of grid points is created with the numpy meshgrid function.

3. Test every grid point

The distance variations are calculated using equation 2.10 for each grid point. Every new value is compared to the previous one and the highest value is saved after the iteration is complete. The point which creates the highest value is a new CCR point. This process is repeated for each additional CCR to be placed.

2.2.3 Calculation of Surface-Vector

This section is dedicated to the so called "Cone-Approach". The basis of this attempt is to observe the same satellite or space debris simultaneously with two SLR stations. This method is called "bi-static observation". Due to the angular differences of the observation vectors and the different locations of the stations, the resulting differences in the residuals can be used to draw conclusions on the attitude of the space object. The idea is to put the same CCR in the center of origin and to find for each station separately the possible locations for a second CCR. As a result, each possible location lies on a cone, intersected by a plane and resulting in a circle. A circle in 3D space where the other CCR could reside for each station. After the intersection with another, exactly two possible locations for the other CCR remain. Resulting in an ambiguity that can only be resolved by observing with a third station simultaneously. However, observing with three stations at the same time is hard to accomplish. Therefore, this thesis is focusing on merely bi-static and not tri-static observations and deals with the ambiguities. The result of this approach are two surface vectors observed over the whole pass. Therefore, conclusions on the attitude of these surface vectors may be drawn.

The data needed to perform the upcoming steps are the residuals, CCR position info and the observation vector. First, the residuals to each single CCR are needed from two different stations. They can be obtained by simulation or observation. Furthermore, the epoch in seconds of day (SoD) is needed to perform as time-step and time variable in general. Secondly the CCR positioning file containing the exact position of each CCR relative to the CoM of the S/C is needed. The final requirement is the observation

vector from both stations given in the same coordinate system. The specific system employed is inconsequential for the calculations themselves. The coordinate system in which the observation vector is defined will be used for all subsequent calculation steps and solutions. Therefore, the choice of the coordinate system is made when passing the observation vector. The most common coordinate system used for describing satellite movements is either the International Celestial Reference Frame (ICRF) or the GCRF. The following steps describe how the so called surface vector is calculated which is needed for the method to work.

Step 1: Place on CCR in der center of origin

The initial step is to define and choose the coordinate system and to shift the center or origin in the position of the first CCR.

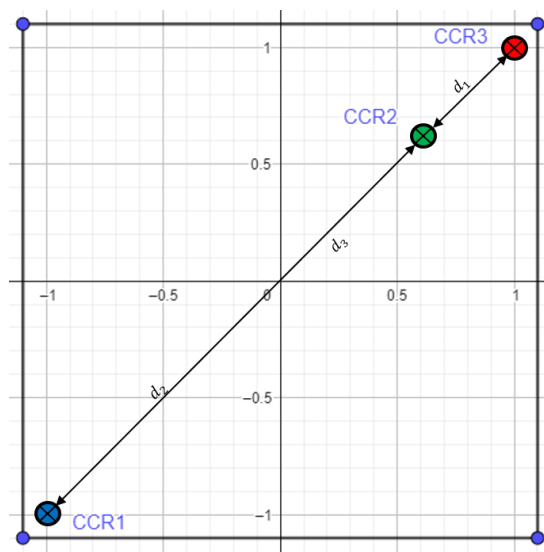


Figure 2.11: Example CCR pattern.

The ICRF is the optimal choice for representing reference data on positions and motions of celestial objects. It has its origin based in the barycenter of the solar system and the axis directions are space fixed, meaning that they do not change over time. The GCRF is a coordinate system that describes the positions and motions of objects in the space

with respect to the Earth. It has its origin at the center of the Earth and comprises a fixed set of reference axes [Ashkenazi, 1986].

Nevertheless, for all subsequent calculations, the origin of the coordinate system is shifted in one of the CCRs position, irrespective of the coordinate system selected initially. However, the direction vectors continue to point in the same directions. This step offers a significant reduction in the complexity of all subsequent calculations.

Step 2: Calculate residual differences

For subsequent calculations the residual differences at every time-step have to be extracted from the data. Of interest are only the differences between the two CCRs, which are further away from each other, as the third CCR in the middle is merely for identification purposes. Examples of three residual differences are given in Fig. 2.12, where Δr_1 , Δr_2 and Δr_3 represent three different extreme states during one revolution each: Δr_1 is the residual difference where the CCRs, on the surface, are first in the FOV, Δr_2 is where the observation vector is perpendicular to the surface, thus the residual differences are zero, and Δr_3 where the CCRs leave the FOV.

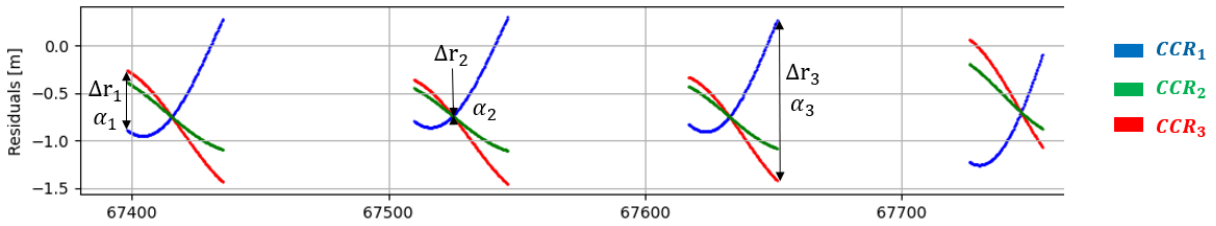


Figure 2.12: Example simulation to extract residual differences.

Subsequently, based on the known mounting distance, d , it is possible to calculate the incident angle, α . Eq. 2.11 presents the mathematical background for these geometric relations:

$$\alpha = \arcsin\left(\frac{\Delta r}{d}\right). \quad (2.11)$$

It is assumed that the observation vector is parallel for all points on the object. In practice, however, there would be a slight angle between them, as these vectors originate from the same point but point to a different point (different CCR). However, the diameter of most satellites is only a few metres at its largest, compared to a few hundred kilometers of observation distance. As a result, the angle variation can be considered negligible and would be significantly smaller than $3\mu\text{rad}$. Following Fig. 2.13 shows the definition of the incident angle, α , which represents the angle between the incoming laser beam vector and a normal vector of the surface.

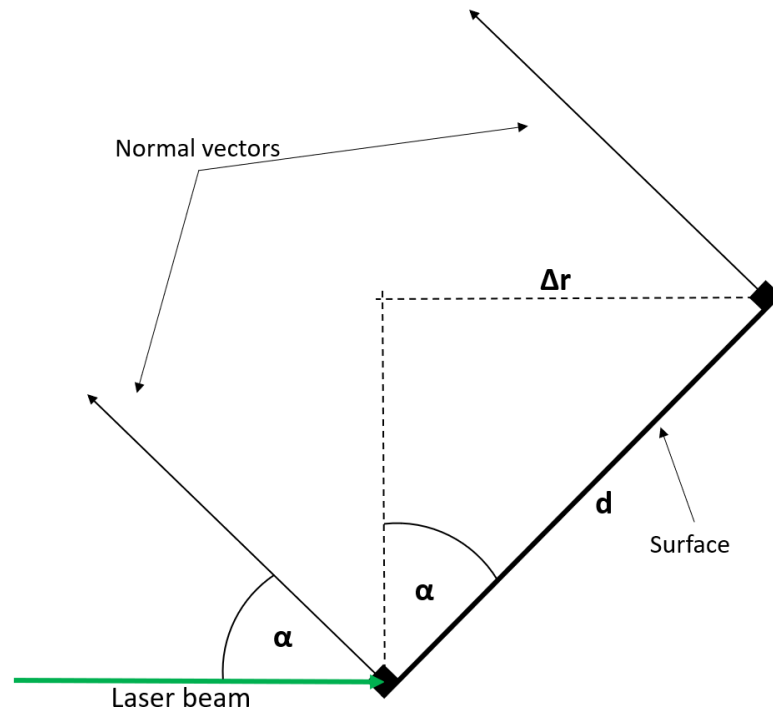


Figure 2.13: Example to explain the incident angle.

This means that if the laser beam would hit the surface at 90° , the incident angle would be 0° . In general, it can be stated that a lower incident angle generates a higher return rate as the cross section is enhanced under these circumstances. All other values will result in a reduction of the cross-section, which will consequently lead to a lower overall return rate, as pointed out in equation 2.5. The described procedure needs to be applied to both stations' residuals individually at every time step.

Step 3: Calculate the radius of the resulting circle

As described in step 1, per definition one of the CCRs is located in the origin. In the example given in Fig. 2.14 CCR_1 is shifted in that point. The idea is to calculate all possible positions of CCR_3 relative to CCR_1 . Also shown in Fig. 2.14 the residual difference, Δr , and the incident angle, α , which were extracted in step two. Since the residual difference is the range difference between two CCRs in observation vector direction, \vec{o}_v . It is known that CCR_3 is Δr "behind" CCR_1 . It is mandatory that each and every CCR is identified, since the mounting distance, d , between them is required for the subsequent calculation. In section 2.2.2 the method to distinguish each CCR is described and by applying the trigonometric relations in following equation 2.12 the possible location of CCR_3 can be estimated:

$$R = \sqrt{d^2 - \Delta r^2}. \quad (2.12)$$

Assuming that the observation vector, \vec{o}_v , is parallel to all points on the surface it is known, that CCR_3 has to be on a plane which is perpendicular to \vec{o}_v and is Δr "behind" CCR_1 . In fact, it lies on a sphere with a radius of hundreds of kilometers, but the differences are negligible. Based on geometric relations it is possible to create an imaginary cone, showed in Fig. 2.14, which is then intersected with the CCR-plane. The cone angle is 90° minus the incident angle, α . The intersection curve, *green*, is the curve on which CCR_3 must reside. To calculate the radius, R , of the resulting circle, equation 2.12 can be used. This step has to be done with both stations at every epoch, too.

Step 4: Calculate the interception of both circles

When the steps 1-3 are done for both observing stations the two resulting circles can

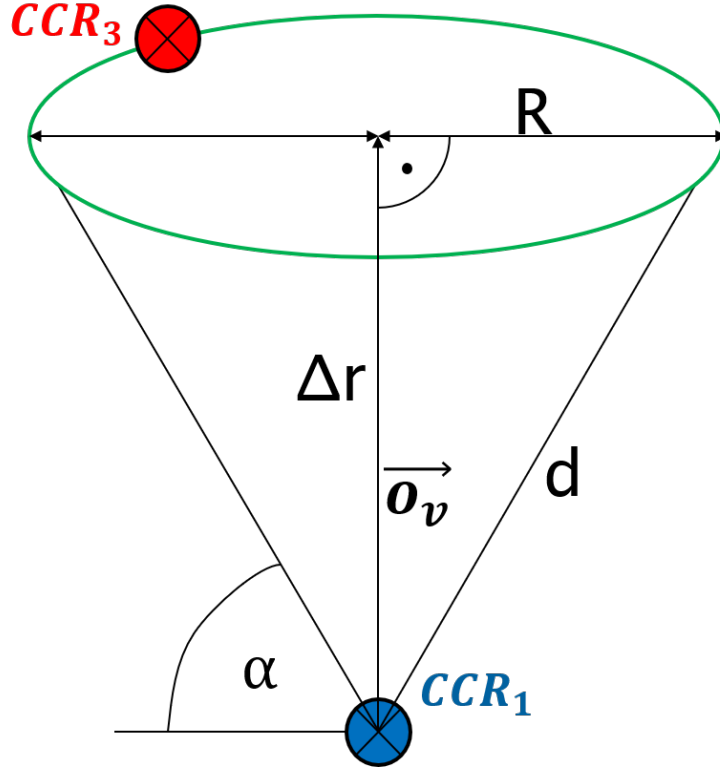


Figure 2.14: Principle of the cone approach.

be intersected. It is important that in step one the same CCR is shifted into the center of origin in both observations/simulations. The intersection points are calculated using the least squares method because inaccuracies can be equalized to a certain degree. In general the least square method is searching for the points where the two circles are closest together within a certain margin. In the majority of instances, the calculation results in two solutions, even though in some cases, a single solution is produced if the circles intersect at a single point. The intersections are presented in Fig. 2.15, where they are marked with $CCR_{3,1}$ and $CCR_{3,2}$. The two cones originating from CCR_1 are marked in the colors *green* and *violet*. The vectors which link the CCR_1 with the potential locations of CCR_3 are called surface vectors, \vec{v}_1 and \vec{v}_2 . As the name suggests the surface vectors lie on the surface on the S/C and point from one CCR to another.

Based on the behaviour over time conclusions can be drawn on how the orientation of the surface changes. There are ambiguities due to the two possible points of CCR_3 which

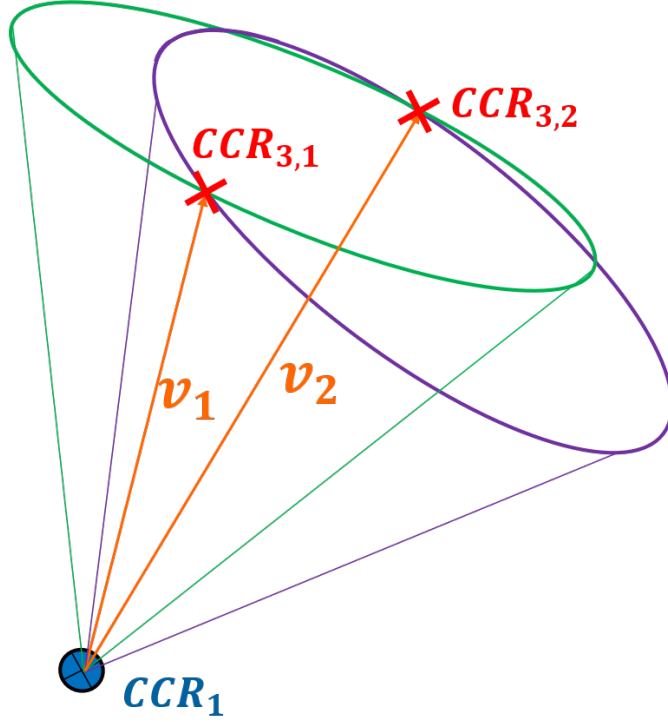


Figure 2.15: Cone idea with two SLR-Stations.

is resulting in two surface vectors. Nevertheless, when the calculations continue it is taken into consideration that one of the two results may be misleading. For the calculation of the possible location of the CCR_3 two planes, p_1 and p_2 , and one sphere, s , are intersected using the least square method, graphically illustrated in following Fig. 2.16.

The first plane, p_1 , is defined by the normalized observation vector of station one, $\hat{\mathbf{o}}_{\mathbf{v}_1}$ and the residual offset from the origin CCR Δr_1 . This is presented in following equation 2.13. The unknown position points, represented by the vector \mathbf{s} , are to be solved by using the given equation and is defined: $\mathbf{s}_1 = [x, y, z]^T$,

$$p_1 = \hat{\mathbf{o}}_{\mathbf{v}_1} \cdot \mathbf{s}_1 - \Delta r_1. \quad (2.13)$$

The equation for the second plane is similar to the first plane, but uses the observation vector and the residual differences from the second station, see equation 2.14,

$$p_2 = \hat{\mathbf{o}}_{\mathbf{v}_2} \cdot \mathbf{s}_2 - \Delta r_2. \quad (2.14)$$

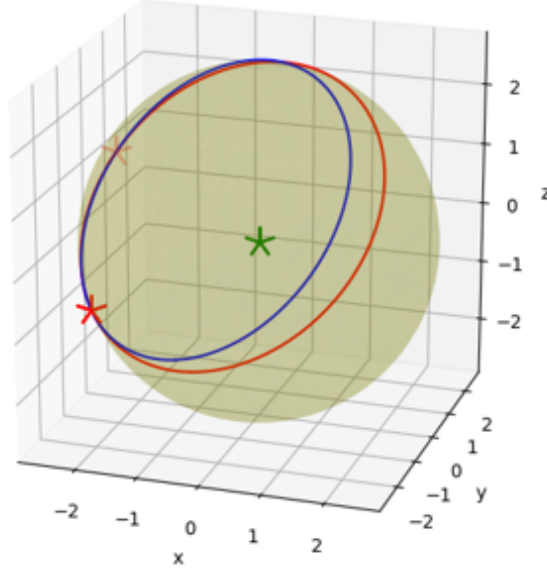


Figure 2.16: Graphical result of the intersections of the two cones / spheres.

The third equation 2.15 is necessary so solve this set of equations with three unknowns. It is describing the sphere with a shift by the mounting distance, d , between the two CCRs,

$$s = \sqrt{x^2 + y^2 + z^2} - d. \quad (2.15)$$

The set of equations is then solved with the "scipy.optimize" library in Python using the "least_squares" function. The initial points for the calculation are chosen arbitrarily. The solution is only valid if the margin is lower than 10^{-6} m. A graphical solution of this calculation is shown in Fig. 2.16, where the green star represents the CCR_1 in the center of origin and the red star the two solutions for the position of CCR_3 .

Step 5: Interpretation of resulting vector

As explained in step 4, the surface vector, \mathbf{v} , is located on the surface of a S/C and is connecting the three CCRs on it, CCR_1 , CCR_2 and CCR_3 . Fig. 2.17 represents a

schematic of the data acquired from the past steps. The vector has a certain distance, d_n , from the center of mass (CoM) and \mathbf{v} is given in the same coordinate frame as the observation vector is defined in. Now, \mathbf{v} can be calculated at every time step the CCRs are within in the FOV. Its is important that this vector is not describing the rotation axis, RA , as this axis has to pass through the CoM and the surface vector is not. However, the change of \mathbf{v} is describing the rotation of this vector on the surface around the rotation axis, thus, the surface and the whole S/C, too. The steps 1-4 can now be iterated over the whole pass. Phases where no CCR is visible will be filled up with NaN values. This occurs when the CCRs are not in the FOV.

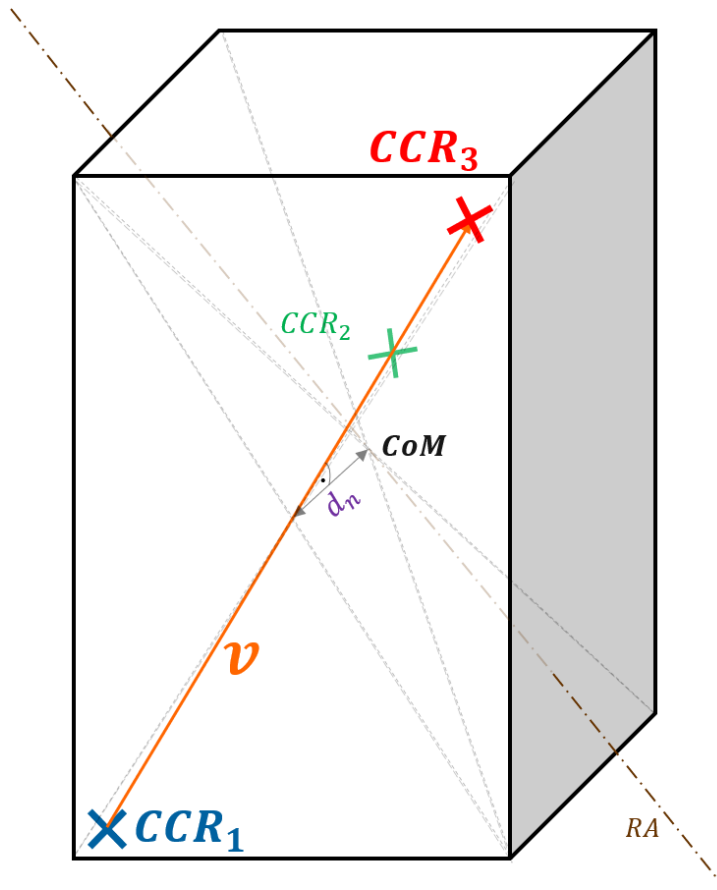


Figure 2.17: Schematic cone idea on a S/C.

2.2.4 Data Editing

When a S/C passes over a SLR-Station and is rotating, not at every time a face with CCRs will be visible from the station. Depending on what the rotation axis and the rotation period are, the same face could be visible a number of times during a pass. This is shown in a example simulation in Fig. 2.12, where a simulated pass of TechnoSat with three CCRs on one face is presented. During the pass, the CCRs are visible four times, or at least they are within the FOV. While the CCRs are visible, the simulation produces data which is stored in an extra output file. When they are not visible NaN values will be saved correspondingly to the specific time step (epoch). To further analyse the data some data editing is necessary. First of all, the surface-vector has to be simulated over the whole pass, the method is explained in 2.2.3, afterwards the following four editing steps must be performed.

Step 1: Chunk the data

The initial stage of the process is to divide the data into discrete units, or chunks, for storage. This includes the creation of a separate record for each instance a face is visible. In the example of Fig. 2.12 this would lead in four parts each representing one revolution. As previously stated, instances where no CCR is visible will result NaN values. Consequently, the data can be separated into distinct segments based on the presence of these gaps. The NaN values can be simply found by using following python command line:

Listing 2.3: Find NaN values

```
nan_indices = np.where(np.isnan(data))
```

After this step we can analyse each chunk separately, for example the one with the time slot ≈ 67380 sod to ≈ 67440 sod. Consequently, a chunk is the part of a pass when a face of a S/C is continuously visible, an example chunk is plotted in Fig. 2.18.

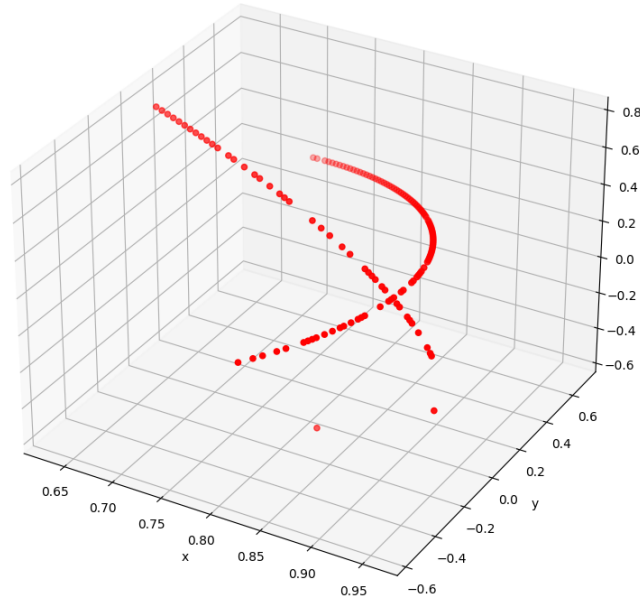


Figure 2.18: Example of a single chunk.

Step 2: Separation of the curves

Given the ambiguity that arises from the existence of two solutions, it is necessary to separate the two curves resulting from the propagation of the surface vector over the entire pass. In Fig. 2.18 such a chunk, which is a combination of the two solutions, is outlined. Visually, the two curves can be clearly recognized and distinguished from the other, however, a Python script is developed to separate the curves automatically. The dots are the positions of CCR_3 and the vectors from the origin (CCR_1) to the points would be the surface-vectors at every time-step. In order to separate the curves some steps need to be done:

- Outlier removal

The initial step is to remove any outliers, as the subsequent stages require the construction of a vector from one point to the next neighboring point. It should be noted, that a single point could also be misinterpreted data as well. By default, an outlier is identified if it has no neighbour in a proximity of less than 0.1 m.

- Choose initial point

In order to perform the interpolation, it is necessary to select a point which will serve as the starting point for the process. From this initial point, the next point on the curve can then be identified. The optimal solution would be to identify a point at the border, however, any arbitrary point is acceptable, with the understanding that more iterations would be required.

- Euler Step Interpolation

A vector is created from the second-to-last point to the last point, with its origin shifted to the latter point. The new point is situated in closer proximity to the tip of the vector than to the original last point. This method necessitates the identification of the initial two values, whereby two points are required to construct the vector. The default value of the length of the vector is set to be 0.01 m. Accordingly, the direction in which the new point should be recognised is predetermined. This is particularly important when two curves intersect. However, under the given circumstances this is not always sufficient to achieve an acceptable solution. Consequently, an additional technique, called cone filtering, is applied.

- Cone Filtering

To obtain a stable solution a cone is constructed around the vector, excluding all points that fall outside of the cone. Therefore, they are not considered for subsequent analysis. The opening angle is defined by the ratio between the distance in longitude direction and the normal distance to the vector: $\frac{l_{dis}}{n_{dis}}$. By default, the ratio is set to be larger than 25.

- Proximity

Here the objective is to identify the data point closest in proximity to the Euler step point. In the event that no point is located within the specified proximity range (by default 0.1 m), the curve which is identified so far is saved.

- Result

In the end of those steps, it is possible that more than the targeted two curves remain. However, the curve segments which are identified with this method will be combined in the next step.

Step 3: Combine Sections

To combine the sections a spline of a certain degree is fitted through the data points of one section. Considering the underlying data set the best results are obtained with splines of degree 1, 3 or 5. The applied spline is extended to reach the other sections and the mean normal distance (standard deviation) of the other sections to the just created spline is calculated. This was done by implementing a Python function which finds the shortest distance from every data point to the just created spline.

Listing 2.4: Find closest curve

```
def closest_point_on_curve(point, tck, num_points=1000):
    u_fine = np.linspace(-3, 4, num_points)
    curve_fine = np.array(splev(u_fine, tck)).T
    tree = cKDTree(curve_fine)
    dist, idx = tree.query(point)
    closest_point = curve_fine[idx]
    return closest_point, dist
```

The input parameters are as follows:

1. "point": Target point of one spline where the shortest distance to another spline is searched for.
2. "tck": The curve in a B-spline form.
3. "num_points": The number of points required to generate the curve for the purpose of identifying the data point in the closest proximity. The default is 1000.

The first step is "u_fine", which generates an array in which range the curve should be created. Next, "curve_fine", evaluates the B-spline and computes the splines value at each of the points. "cKDTree" constructs a k-d tree which allows for efficient spatial

searches within the curve. The outputs of "tree.query(point)" are the shortest distance to the spline from "point" and the index. By using the index, the closest point can be identified.

When another section is found within a certain proximity to the spline, the sections can be combined. The default value for the allowed standard deviation is 0.3m. If no other section within a given proximity is found, the same procedure has to be repeated but with another section. This process should be repeated until only one or two sections remain. If there is only one solution and no ambiguities, one section will remain. If there are two solutions, with one being incorrect, two sections will remain.

Step 4: First Visualization

With only one or two sections left, another spline can be created to visualize the approximate rotation. Two splines are therefore created using the data of both remaining curves. They will be extended to visualize the approximate rotation. They, however, will always show the rotation of the surface-vectors, v_1 and v_2 around the rotation axis and not the rotation of the space object itself. Also the result of the spline will not be a perfect circle because of the introduced rotation due to the orbital movement. What can be observed from the ground is the apparent rotation, whereas the S/C experiences the true rotation. The shift in the rotation, which will look like a spiral in the results, is the part of the introduced rotation due to the propagation on its path around the Earth.

3 Results and Discussion

3.1 Satellite Laser Ranging

In this section the results regarding the SLR residual simulation tool will be discussed. At first, the result of a basic SLR simulation and explained and secondly a case study is shown which verifies that bi-static SLR observations are possible and useful for further analysis.

3.1.1 Basic SLR-Simulation

To be able to understand and interpret the outcome of the simulations it is important to know the output format of the simulation and the information given. In Fig. 3.1 an example for a result file with detailed explanations is shown. In the top left corner the main information and preferences are stated. Information about the pass and the rotation parameters can be retrieved there. A sketch of the spacecraft with its CCRs and their corresponding normal vectors is illustrated in the top right corner of the output file. The actual residuals are positioned below the main preferences and the sketch, with each color representing multiple CCRs from one face. In the bottom of the output page the elevation and the angle between the observation vector and the rotation axis are plotted.

In addition to the graphical output file, further files are created during the simulation process. This allows further calculations using these results, rather than simply examining them visually. The additional output files are listed below.

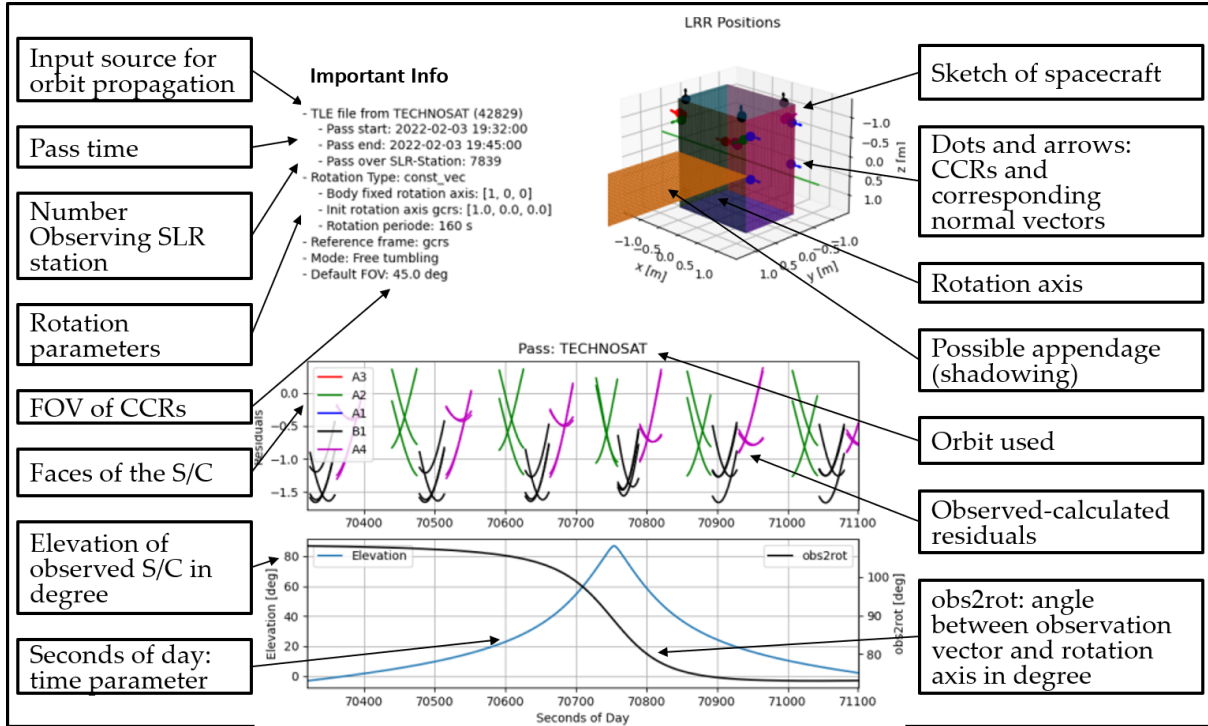


Figure 3.1: Example SLR output file with description.

- **Residual-File:** This file not only contains the residuals at every time step (epoch), but also the most important information for post processing applications. It contains the information on the pass which is simulated. Therefore, the NORAD-ID of the observed S/C with the start and end time of the observation as well as the used TLE file for the simulation. Next, rotation parameters like the rotation axis, rotation period and the reference frame are given. Finally, the CCR position, orientation data and FOV are stated in this output file.
- **Quaternions:** The quaternions of every axis as well as of the rotation itself with its initial value are included in this file.
- **Json-file:** The applied Json-Input-file to retrieve every information of the simulation tool.

3.1.2 Bi-static SLR Simulation

A simulation of two distinct stations was created to demonstrate the feasibility of bi-static measurement and its potential for generating valuable results. To this end, two stations were selected to simulate residuals for a TechnoSat pass. The two stations, SLR-Station Graz (Austria) and Wettzell (Germany) are situated approximately 300 km apart from each other, allowing the observation of the same satellite within the same atmospheric envelope. In Fig. 3.2 the residual simulations are shown: The top graph displays the residuals of the Graz simulation, while the middle graph depicts the residuals of the Wettzell simulation. In those simulations the same pattern of three CCRs in a straight line was used, where the outer CCRs, blue and orange, are approximately 2.8 m apart. The x-axis represents the seconds of day (SoD), which function as the time variable. The y-axis is the simulated residual offset in relation to the CoM of the S/C. At first sight, both simulations look similar with just minor differences, and have the same behaviour of the residual pattern. However, by looking at the bottom graph significant variances are recognizable. The colored lines represent the absolute differences between the residuals from the data gathered by both stations. The residual differences are calculated for each CCR individually. The range differences to each CCR are significant, reaching a maximum of approximately 50 cm. In general the SLR accuracy is below one centimeter, thus, in theory it should be possible to observe considerable range differences throughout all passes.

Fig. 3.3 shows the azimuth and elevation of a satellite observed from the same two ground stations (Graz, Wettzell) over the common pass. Only the parts of the pass where both stations are able to observe the S/C are plotted. The first two plots show, separately for each station, the azimuth and elevation angles as functions of time (SoD). The third plot shows the differences in these angles between the two stations.

The blue line indicates the azimuth angle, which represents the horizontal direction. This angle slowly changes with time when the satellite is in motion. It increases from

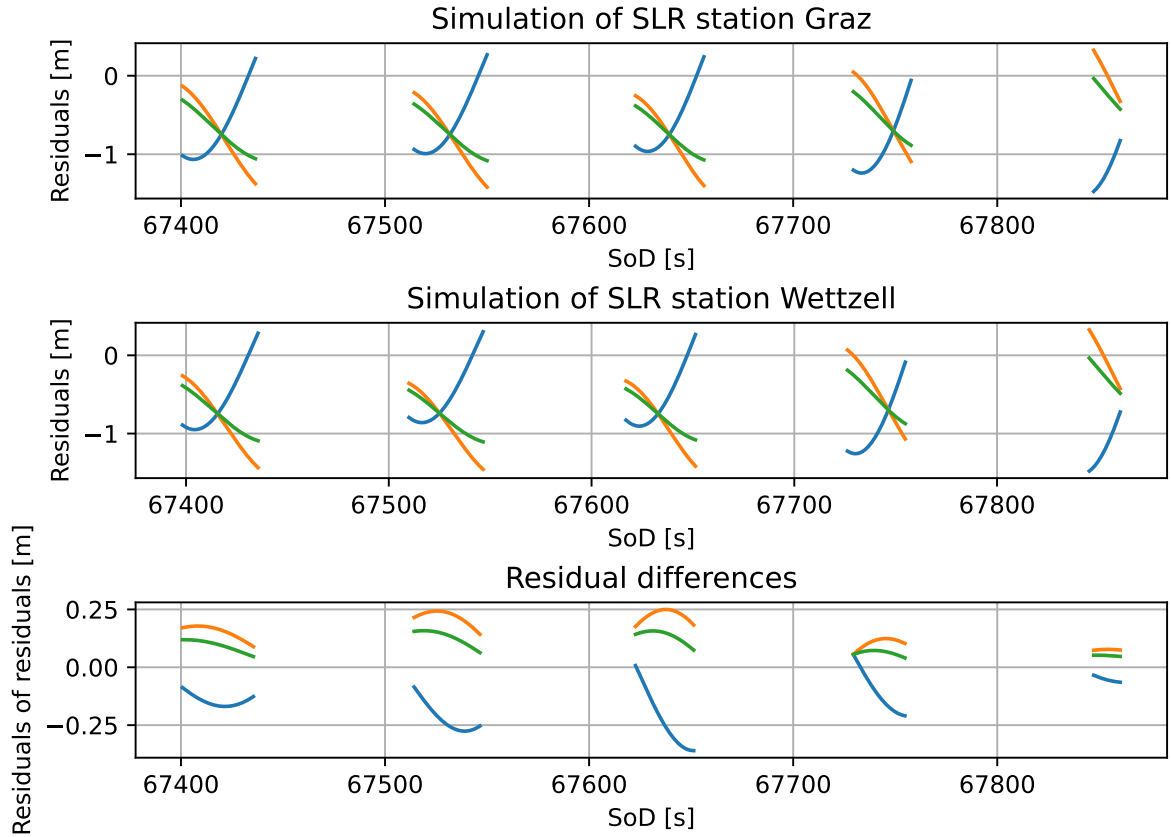


Figure 3.2: Simultaneous observation simulation: Residuals. One color represents one CCR and the color code is the same for all three plots. Blue: Single CCR further away from the others; Orange: CCR furthest away from the blue one, but paired with the green CCR; Green: CCR between orange and blue but closer situated to the orange CCR.

its low value over the horizon in the north (0°), then rises closer to its zenith when it is east (90°) of the station. After its descend it passes the horizon in the south (180°). The azimuth angle has the same behaviour in both simulations with minor differences.

Also the elevation angles, represented as red line, show similar behaviour. As expected the elevation starts at almost 0° , when it rises above the horizon. Subsequently, it gradually ascends to reach its peak, the zenith. In this instance, the highest point of the observed satellite is just above 30° elevation. A comparison of the first two graphs reveals that Wettzells' observation reaches its peak approximately 20 seconds before Graz'.

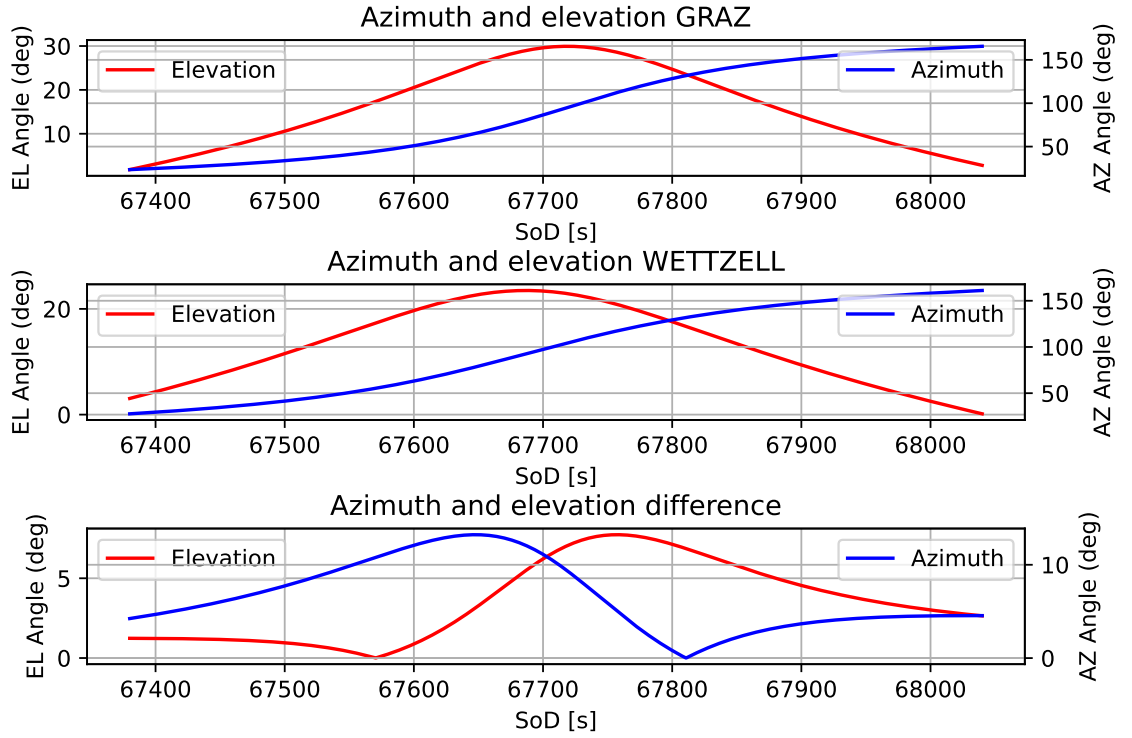


Figure 3.3: Simultaneous observation simulation: Azimuth and Elevation angle.

After reaching the zenith both descend until ultimately reaching the horizon. Another interesting observation is that the Wettzells simulation starts at an elevation angle of approximately 5° . In contrast, the Graz' simulation ends at an elevation angle of about 3° . In general the simulation should start and end at an elevation angle equal to 0° . But as stated in the beginning of this paragraph, only the parts where both stations are able to observe are plotted. In conclusion, it can be stated that the Graz station had the advantage of observing the S/C at an earlier point in time than the Wettzell station and for a longer period. This is also evident with the azimuth angles, as the pass is primarily east of Graz station and Wettzell is situated to the north-west of Graz. Consequently, the S/C was closer to Graz station than Wettzell throughout the pass. This is also reflected in the lower maximum elevation angle of both stations. While Graz's maximum value is approximately 31° , Wettzell has a maximum of just approximately 23° .

In the last graph the direct comparison of both stations is shown. When looking at the elevation it is interesting that firstly the elevation of Wettzell increased faster until Graz overtook at approximately 67,570 SoD. After that the elevation of Graz was always higher. As the S/C came from the north direction, Wettzell was able to detect it first. Therefore, the azimuth angle was almost zero (north) when Wettzell started to detect the S/C and Graz's azimuth angle was already at about two and a half degrees. As the azimuth angle rises faster for Graz's observation it ended up with a larger end azimuth angle of the same about at it was lower in the beginning. The reason for this discrepancy is that the two stations are situated at a considerable distance from one another, approximately 300 kilometers, which is

3.2 Attitude Conclusions based on single SLR-Station

On the basis of single station SLR-Simulations some conclusions can already be made regarding the attitude. Thereby specific points in the (simulated) residuals can be used, for example the points where all CCRs of one face have the same residuals. This occurs when the surface is perpendicular to the observation vector. In the case that four CCRs are placed with an adequate mounting distance between them, the points in question can be utilised in a manner similar to that of two CCRs with the same residual, while the other two have different but equal residuals.

3.2.1 Apparent Rotation depending on Elevation

The apparent rotation or retrograde motion of a space object is the rotation in the opposite direction of the orbit itself. Due to the propagation in its orbit one rotation by revolution will be introduced on the S/C. The number of apparent rotations are the rotations an observer would count by looking at the S/C from Earth's surface. The observer is, thereby rotating with the Earth or the S/C around the observer. In contrast, the number of true rotations would be determined if the observer would observe the satellite from a distance

in the vast expanse of the universe. Depending on the rotation direction of the S/C the apparent rotation therefore can be larger or lower than the true rotation when observed by a station on ground. In Fig. 3.4 an example simulation is made where the apparent rotation period can be extracted from the residual data. In the top graph the residual simulation is shown with four different apparent rotation periods marked in red. In the bottom graph the corresponding elevation angle (blue) and the angle between the observation vector and the rotation axis (black) is plotted. In this example a TechnoSat pass with a relatively low maximum elevation of 43° was chosen. The rotation axis is $[1, 0, 0]$ object fixed and the (true) rotation period is 180 s.

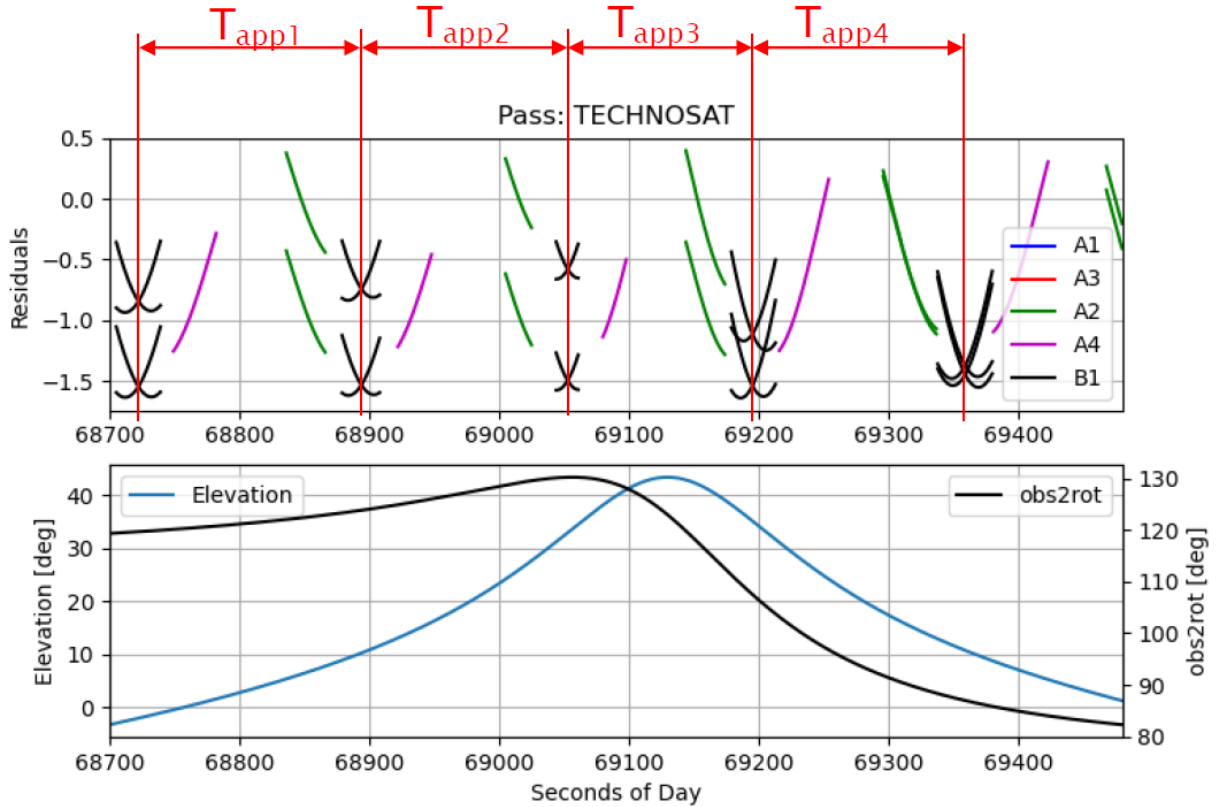


Figure 3.4: Apparent rotation depending on the elevation. The A1 and A3 faces are not visible because in this rotation those faces were never visible to the observing station.

In this case the time for each revolution of the S/C is compared. For the spacecraft itself each rotation would take the same time, because the rotation period is constant.

However, for the apparent rotation the elevation angle from which it is observed from the ground is important. The higher the elevation angle, the higher is the relative speed between the S/C and the ground station. This effect is observable in Tab. 3.1, where the results of the apparent rotation measurement from Fig. 3.4 is shown. It points out that the deviation from the true rotation (180 s) gets larger the higher the elevation is. Whereas the deviation in case T_{app1} is just 9 s or 5 % with an average elevation of $\approx 5^\circ$, the part with the highest elevation ($\approx 40^\circ$), T_{app3} , has a variation of 38 s, or 21.1 %.

Table 3.1: Results of the apparent rotation variation

	Apparent Rotation	Absolut Deviation	Relative Deviation
T_{app1}	171 s	9 s	5 %
T_{app2}	159 s	21 s	11.7 %
T_{app3}	142 s	38 s	21.1 %
T_{app4}	164 s	16 s	8.9 %

The reason for that behaviour could be, that the relative velocity between the station and the S/C is higher, if the elevation is also higher. This means, that in the same time the S/C covers a larger propagation angle when the elevation is high, covering a larger circular segment in the same time. Therefore, the retrograde motion effect comes more into count, than with a lower elevation angle.

3.2.2 Incident Angle

The incident angle, α , describes the orientation of the surface relative to the laser beam, therefore, the observation angle. It can be described as angle between the laser beams and the surface of the target. To calculate the incident angle based on the residuals the CCR positioning has to be known. By using the central residual distance of the intersection between two crossing CCR residual lines. It can be calculated following equation 3.1. Meaning, two CCR have the same distance to the SLR station in both cases. The central residual distance is r and the mounting distance is d ,

$$\alpha = \arcsin\left(\frac{\Delta r}{d}\right). \quad (3.1)$$

When applying Eq. 3.1 in the residual simulation in Fig. 2.12 the incident angle for this three example points can be calculated. In our case study the mounting distance between the two outer CCRs, CCR_1 and CCR_3 , is: $d = 2\sqrt{2} \approx 2.38 \text{ m}$. The results of the estimated incident angles are shown in Tab. 3.2. By utilizing the incident angle, it is feasible to determine a portion of the orientation of the S/C. However, it is important to note that this method only reduces the possible orientations in 3D space by one dimension, as the surface is free to rotate around the observation vector, thereby creating a cone of potential orientations. Nevertheless, this part is crucial for the development of the cone idea, which is described in section 2.2.3.

Table 3.2: Results of the Incident Angle

	α_1	α_2	α_3
Δr	0.53 m	0 m	0.75 m
Result	10.8°	0°	15.38°

3.3 CCR Placement Differentiation

The numerical solution from equation 2.10 in section 2.2.2 shows, that the best position of three CCRs on a rectangular surface is on a straight line where two CCRs are situated in the corners. In this example the exponent p was chosen to be two. A schematic of the result is illustrated in Fig. 3.5. The size of the rectangle is neglectable as the distances are given in multiple of the diagonal. The red and the blue CCR have the maximum distance possible, the diagonal d of the rectangle. The green CCR is situated $\approx \frac{1}{5}d$ and $\approx \frac{4}{5}d$ away from the red and blue CCR, respectively.

This CCR pattern was then simulated with the SLR-Simulation Tool which is described in 2.2.1. In the case study a noise of 3 %, a rotation period of 120 s around the axis $[1, 1, 0]$ was added. The edges of the surfaces were chosen to be $a = 3 \text{ m}$ and $b = 4 \text{ m}$, so the diagonal would be $d = 5 \text{ m}$. If the Center of Origin (CO) is placed in the center of the rectangle the position of the CCRs would be: $P_1 = (-2, -1.5)$, $P_2 = (1.13, 0.84)$ and

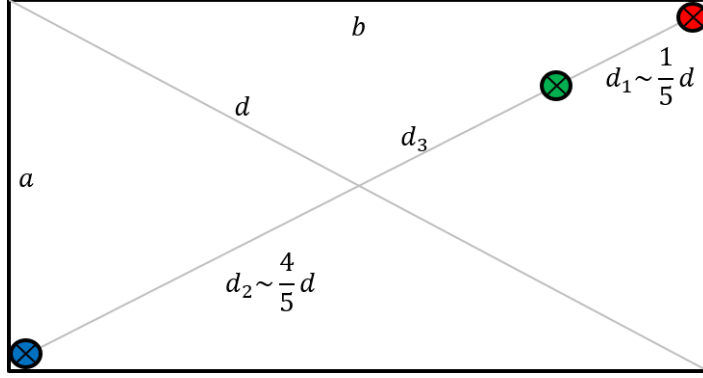


Figure 3.5: Best estimated CCR placement according to simulation on a rectangular surface. Color code equals Fig. 3.6

$P_3 = (2, 1.5)$. Therefore, the distances are: $d_1 = 1.06$ m, $d_2 = 3.94$ m and $d_3 = d = 5$ m. It can be observed, that the two CCRs mounted in closer proximity (green and red) remain closer within the simulation than the third CCR (blue). Consequently, in all rotation states except those in which all CCRs are at precisely the same distance from the station, the blue CCR can be distinguished from the others due to its separation from the others. When the observation vector is perpendicular to the surface, the CCRs are at the same distance from one another. The fact that all CCRs lie on a straight line allows the conclusion that it is impossible, that the green CCR is further away from the blue CCR, in any state, than the red one. As a result, the green CCR is always between the red and blue CCR, or on the same place if the observation vector is perpendicular to the surface.

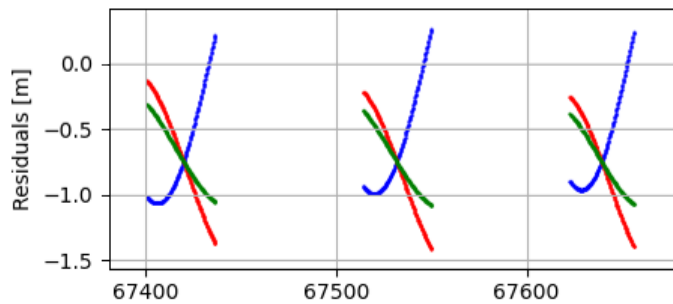


Figure 3.6: Best estimated CCR placement according to simulation on a rectangular surface. Color code equals Fig. 3.5

Thus this pattern allows for the identification of every single CCR, if the quality of the SLR measurement is sufficient to separate the residual lines. If the observation vector is nearly perpendicular to the surface, the differentiation becomes difficult as the residual distance between the CCRs is too low to separate them. This method is only applicable if there are precisely three CCRs mounted in a linear configuration. The introduction of an additional CCR, or a deviation from the linear arrangement may result in ambiguities.

3.4 Surface-Vector

To analyze the behaviour of the surface vector, it is important to calculate it over the whole pass. As the result is a mixed data set, due to the ambiguities further data editing is necessary to extract the data of single revolutions and separated solutions.

3.4.1 Surface-Vector over whole Pass

To explain how the surface-vector will propagate over a whole pass the example below shows a pass of TechnoSat with a rotation period of 120 s around the $[1, 1, 0]$ axis defined in GCRF. The noise amplitude is 0.025 and the FOV of the CCRs is 40° . The outcome of the SLR-Simulation of this pass is presented in Fig. 3.7.

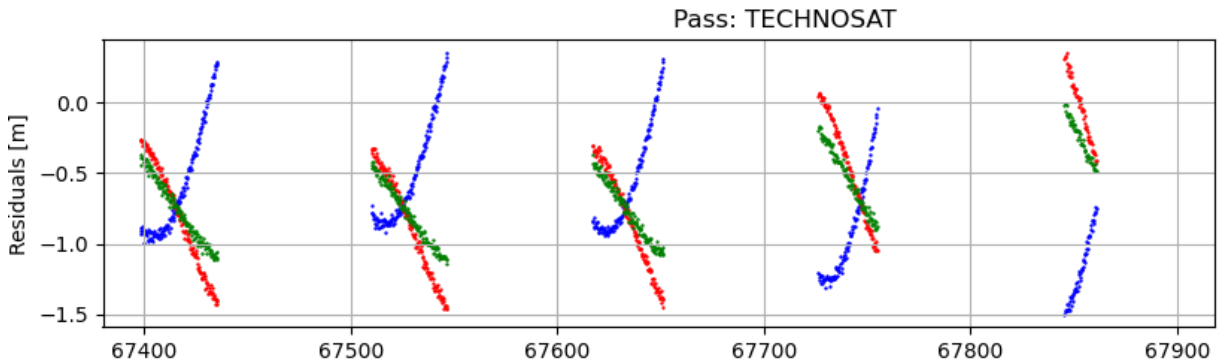


Figure 3.7: Example residual data with noise to visualize surface-vector over time.

When all listed steps in section 2.2.3 to calculate the surface vector for every time step are finished, further data editing is needed to be able to work with the data. First of

all, the data has to be combined, which illustrated in Fig. 3.8. On the left side, all the surface vectors of the entire pass are plotted. The red and blue arrows represent the two different solutions for the surface vectors. To avoid confusion regarding the vectors, on the left side, the same graph is shown but only with the tips of the vectors. These points represent the possible positions of the third CCR. As a reminder, the origin of the vectors is the first CCR, which position was shifted into the center of origin.

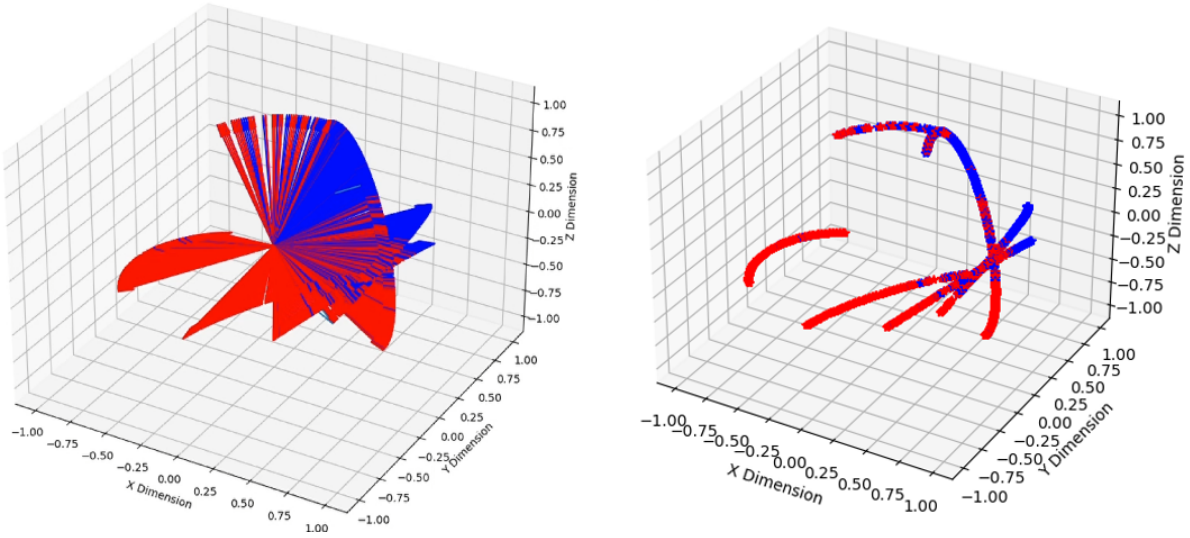


Figure 3.8: Example residual data with noise to visualize surface-vector over time.

On the left graph different segments, can be observed, which visually belong together. However, it is obvious that the single section not only contains one solution but, in most cases, is a combination of both. This is recognizable by the different colors. In the simulation, it is clear which data point belongs to the first and which to the second solution, but in reality, this is not possible. Therefore, it is important for the next step to investigate this problem in depth. Would there be only one solution, then the graphs in Fig. 3.8 would all be in one single color. This is now a mixed dataset and it is not possible to just separate them by position in the solution array. The method used for separating the two solutions in the dataset is described in section 2.2.4.

3.4.2 Data Editing

This sections shows the data editing done with a case study given in section 3.4.1. The following list shows step by step what is done and how it manipulates the data set.

Step 1: Chunk the data

The first step is to chunk the data, which mean so separate them by epoch, so that the data for each rotation can be analysed separately. In this example, the data can be separated in ten individual chunks, because the face of the S/C, which contains CCRs was ten times visible throughout the observed pass. This means that the S/C rotated approximately ten times as well. Four of the chunks are given as examples in Fig. 3.9. However, for the next step a closer look will be taken at the "Chunked Data Part 1", which is larger in Fig. 3.10 on the left side. In this example, the two curves are clearly distinguishable and represent both solutions. However, the process of separating the two curves requires additional data editing, as it is not straightforward to differentiate the data points, particularly at the intersection of the two curves.

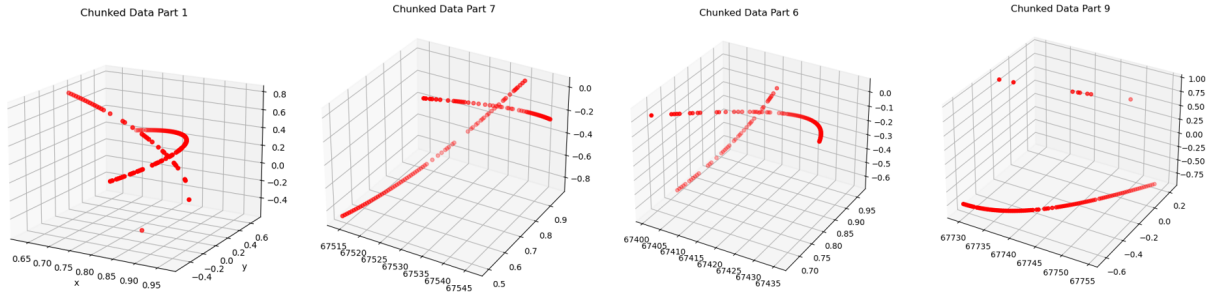


Figure 3.9: Data separated in chunks.

Step 2: Separation of the curves

To be able to separate the datasets additional calculations are necessary (cf. section 2.2.4). First, the outliers will be removed, which in this case are for example to two

data points at the bottom of the graph. This is done, because now two initial points within a certain proximity are chosen, favourable at the beginning or ending of a curve. In most cases these are the two data points at the beginning of the dataset. After that the Euler-step-interpolation and cone filtering is done, and the nearest point is chosen to be the next in this section. This method separates the data in more than two sections, therefore additional steps are required. In Fig. 3.10 the change from the original dataset on the left to the separated sections on the right is shown. The chunk which contains two curves is now separated in six sections, where each section is either part of the first or second solution.

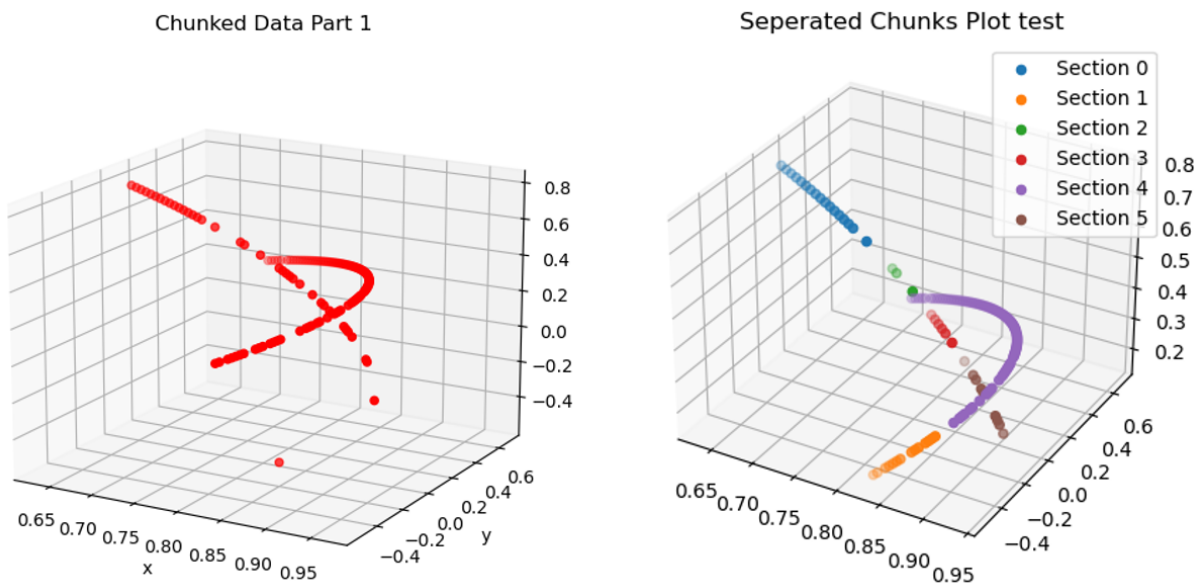


Figure 3.10: Data 1 chunk separated in different sections.

Step 3: Combine sections

To combine the related sections an iteration process is now started. For that reason, a spline which is defined by the first section is created. The spline is extended to reach to the next sections. The spline and the other sections are now compared to determine which section would fit the spline most. The resulting section will be combined with the previous section. This has to be repeated until one or two sections remain. The iteration steps are plotted in Fig. 3.11. For this example, three iterations are needed to get the final result, which is in the lower right corner of the figure.

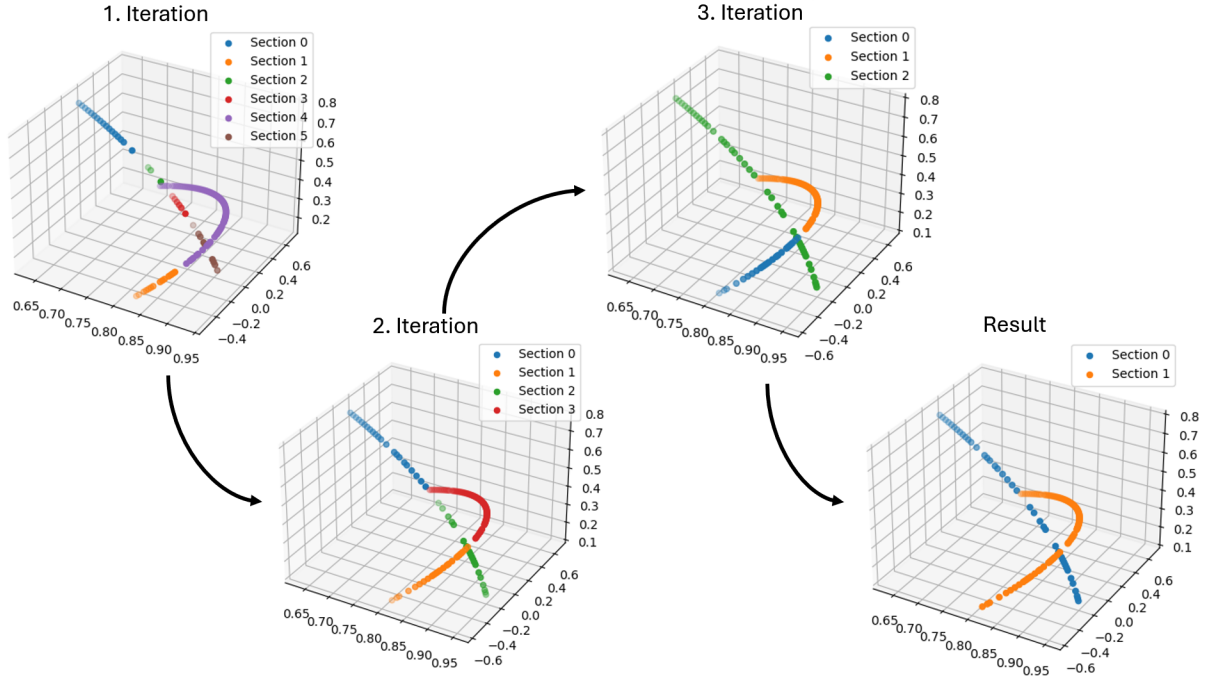


Figure 3.11: All three iteration steps to combine the sections belonging together.

Step 4: Visualisation

Using the result from step 3, a spline can now be created to visualize the rotation of the surface-vectors, v_1 and v_2 . The splines visualize the approximate rotation in Fig. 3.12.

The result of the spline is not a perfect circle, due to the introduced rotation because of the orbital movement, but now the behaviour of a vector fixed to the surface of a S/C is known.

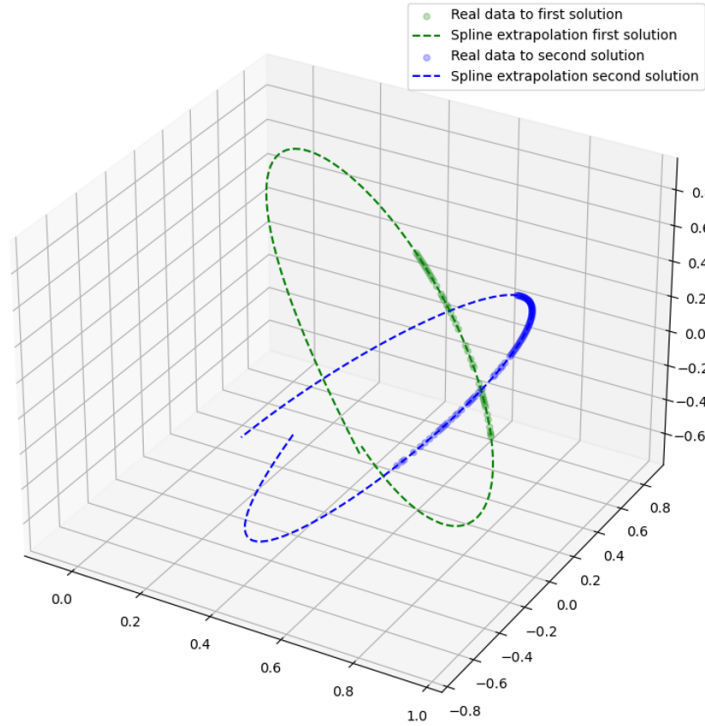


Figure 3.12: All three iteration steps to combine the sections belonging together.

3.5 Attitude Estimation

In this section the attitude estimation based on the attitude of the surface vector is described. For better visualization and understanding the same example pass as in section 3.4 is used. The rotation period is 120s and the rotation axis is $[1, 1, 0]$. In Fig. 3.12 the two possible rotations of the surface vector are shown. Due to the simulation it is known that the first solution, **green**, and the second solution, **blue**, are due to the existence of ambiguities. For the sake of simplification for this section only the first solution is considered.

3.5.1 Rotation Axis

The idea is to form a plane spanned by the possible positions of the second CCR. In this the points in question are the ones of the first solution in Fig. 3.12. The rotation axis is perpendicular to this newly formed plane. However, due to the noisy data and the rotation introduced by the orbit propagation, creating a plane is not trivial. Therefore, a method is introduced to create the normal vector to this plane at each time step and then calculate the average. A visual schematic of the problem is illustrated in Fig. 3.13, where \vec{s}_i are the surface vectors and \vec{d}_i the CCR_{2_i} connecting vectors.

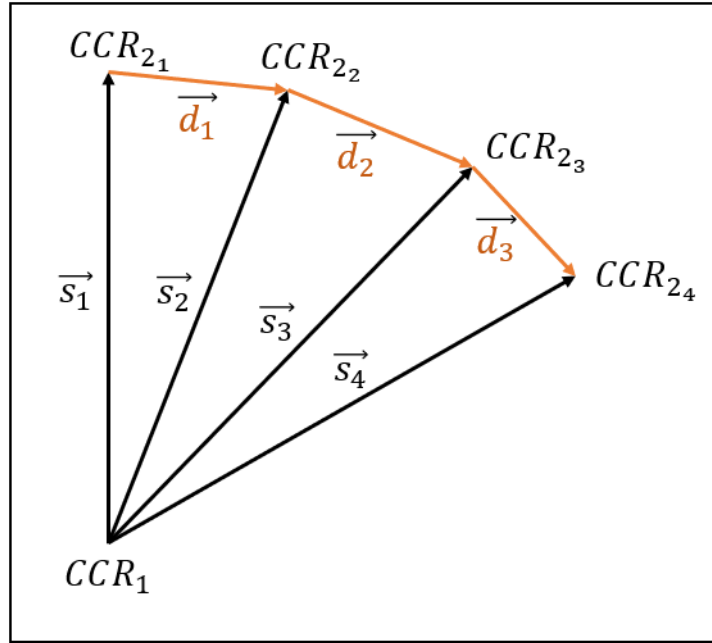


Figure 3.13: Schematic of the rotation axis estimation.

First the vector between the second CCRs, \vec{d}_i , is calculated, by subtracting the corresponding surface vectors, \vec{s}_i . The formula can be seen in following equation 3.2:

$$\vec{d}_i = \vec{s}_i - \vec{s}_{i+1}. \quad (3.2)$$

The next step is to calculate a vector that is perpendicular to the first d-vector and the following. This process yields a vector that is also perpendicular to the resulting plane, thus aligning with the rotation axis, r_a . The calculation can be seen in equation 3.3,

$$r_{a_i} = \vec{d}_i \times \vec{d}_{i+1}. \quad (3.3)$$

Now the rotation axis at every time step can be calculated. To get a more accurate solution, the mean will be calculated. The estimated rotation axis after calculating this steps is: $[0.99637, 0.99992, -8 * 10^{-5}]$. This results in a deviation from the true rotation axis, $[1, 1, 0]$, of less than 0.04 % in x-direction and less than 0.01 % in y- and z-direction. This slight deviation is a result from the noisy data used or a round-off error. The visual solution is shown in Fig. 3.14, the blue dashed pointed line in the actual rotation axis and the orange is the estimated rotation axis. Since the deviations are very small, it is not possible to recognise any differences. However, it can be seen that the rotation axis is perpendicular to predicted surface vector movement.

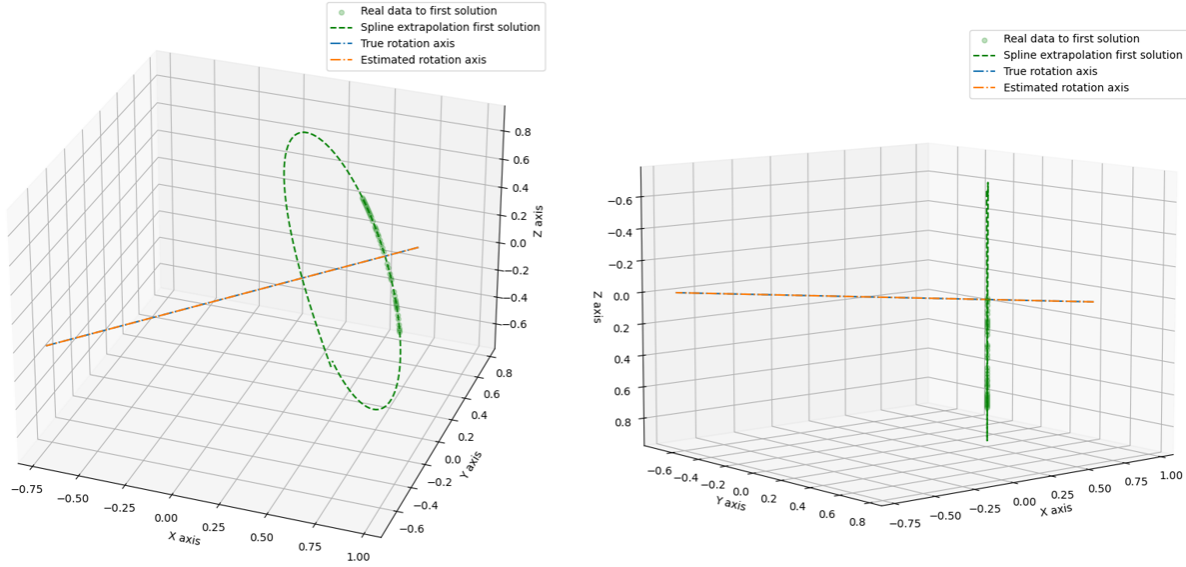


Figure 3.14: Estimated vs. actual rotation axis.

3.5.2 Rotation Period

To finally calculate the apparent rotation period the angle between the surface-vectors can be analysed. Due to the introduced rotation, caused by the propagation in Earth's orbit, the true rotation period cannot be measured directly. Therefore, only the estimation

of the apparent rotation is discussed in this section. If only one station would observe the satellite an attempt to measure the rotation period could be to count the time until the same face is visible again. This would work with simulated data but not with real measurement. In Fig. 2.7, a real measurement of TechnoSat is displayed. It is possible to distinguish between the individual CCRs, although it is challenging to determine the precise moment at which a face becomes visible for the first time. When measuring with two stations the apparent rotation can be determined using the surface-vectors which have already been calculated. Therefore, the angle between two surface-vectors, θ , at an arbitrary time during the visible rotation is needed. It would be beneficial to select two time steps in equation 3.4 that are more distant from one another to enhance the robustness,

$$\theta = \cos^{-1} \left(\frac{\overrightarrow{s[t_1]} \cdot \overrightarrow{s[t_2]}}{|\overrightarrow{s[t_1]}| * |\overrightarrow{s[t_2]}|} \right). \quad (3.4)$$

The angle between the first and the last surface-vector of the same example as in section 3.5 is approximately 45.043° . It took the surface-vector 17.5 s to fulfil a rotation of given angle. Therefore, it will take approximately 139.865 s to do a full rotation. Note that this is the apparent rotation as the true rotation should be 120 s. This results in a deviation of 19.865 s or 16.55 %.

4 Conclusion and Outlook

This thesis shows the feasibility of using Satellite Laser Ranging to determine the attitude of defunct S/C and space debris. Methods for estimating the attitude of space objects are becoming increasingly important as the space researchers need a debris-free space environment to not be restricted in the future. This is necessary so that the objects can be removed from their orbit and to open up the space for new space missions. The European Space Agency also pushes this goal with its statement to be space debris free by 2030. The results in this thesis turns the spotlight on the possibility to perform bi-static SLR observations and shows the potential of targeting at an object from two different perspectives. One of the main findings of this research is, to show the efficiency of the SLR observations regarding the accuracy and the possibility to distinct single CCR in a special pattern on the surface of an spacecraft. This thesis shows that with the special pattern of three CCRs, it is almost always possible to identify every single CCR, except in the case where the surface is too close to perpendicular to the observation vector. The exact placement of the three CCRs is explained in section 3.3, where it is also discussed what the perfect distance between the single CCRs would be. This is an important step to maximize the possibility to differentiate. The introduction of the bi-static SLR simulation also poses a significant information gain, as it became possible to analyse the same pass of a satellite from two different angles. Thus, having two datasets which can be compared to each other. Depending on the variation of these data the surface-vector can be calculated (cf. section 2.2.3). To confirm the feasibility of bi-static measurements simulated residuals from the SLR stations Graz and Wettzell were used.

However, some challenges arise that need to be addressed as well. While introducing the novel "cone approach" to use for bi-static measurements, it was not possible to exclude ambiguities. Consequently, the outcome yielded two potential solutions, one of which was subsequently determined to be an invalid solution. Nevertheless, by using this idea, it is possible to calculate two different states of the surface vector instead of an infinite number of solutions. The idea is, to center one CCR in both simulations and calculate a possible location of another CCR. During the calculation, a cone is created which is intersected by a plane. This creates a circle on which the possible second CCR could be located. The concept is very promising, because it can improve the accuracy of attitude determination based on SLR. Moreover, the cone-based approach results proved that reasonable estimates for the satellite's attitude are possible even with noisy data. This has a wider range of consequences, including the possibility of that multi-station observations which may be even significantly more accurate and probably enabling even real-time updates on rotational states of space debris.

Despite the findings, based on simulated data, in reality the quality of the outcome depends heavily on the accuracy of the SLR stations observation. Furthermore, it is not always feasible to do observations at two different SLR stations at the same time. Since they must be in the same good weather bubble that allows for observations. Stations in closer proximity may experience similar weather conditions, but if they are situated further apart, this may not be the case. Additionally, it is crucial that the stations are not too far away from each other, to ensure the possibility of simultaneous observation.

In the future, further improvements to the solution could be made if the use of machine learning (ML) is analysed. ML can be used not only for data filtering and processing, but also to save time and eliminate the need for manual observation. Another improvement could be tri-static measurements or even multi-static measurements to exclude the

ambiguities. But as mentioned above, if more stations are involved it will get harder to ensure suitable weather conditions at every location. Not only would this improve the overall accuracy but also eliminate the invalid solution.

Looking forward, the methods developed in this thesis have the potential for various applications. The increasing amount of space debris is a growing concern for both commercial and governmental space agencies. Therefore techniques like SLR-based attitude determination will play a vital role in future debris removal missions. The capability to estimate the rotation and orientation of space debris with good accuracy from the ground will be key in the planning of removal missions and collision avoidance. Hence, enabling operational satellites to propagate in orbit without any major collision avoiding manoeuvres. In this respect, the thesis has shown that SLR, especially bi-static SLR, can serve as a feasible and useful tool for attitude determination of both defunct satellites and space debris. Although there is still much work to do, this thesis provides a good basis for taking further actions in this field of research and perhaps in the future it will give a great contribution to space debris mitigation.

To effectively apply the theory in practice, there are still some open questions to be discussed:

- **Ambiguities**

It is debatable whether it is essential to eliminate the ambiguities or is it feasible to conduct meaningful analysis despite these ambiguities? Can the ambiguities be compensated by analyse multiple passes? Is there a possibility to eliminate the ambiguities without a third SLR measurement?

- **Minimum distance between SLR-Stations**

What is the minimum distance between two SLR stations to reach a certain level of accuracy? Is it possible to build a second station just a few kilometers away from the first one? How big would the impact be to the overall accuracy?

- **Timing of the measurements**

It is unclear how the timing of the bi-static measurements is affected by this discrepancy. It is not a straightforward process to conduct simultaneous measurements and accurately correlate the timing. Consequently, it is uncertain how this would influence the accuracy of the results.

- **Other useful applications**

Are there any other useful applications what can be done with bi-static SLR observations?

Bibliography

- [Arnold, 2018] Arnold, D., Retroreflector Array Transfer Functions. (2018)
- [ASA, 2023] "Guide to Space Debris," ASA guide to space debris, 2023, Available: <https://www.spaceacademy.net.au>.
- [Ashkenazi, 1986] Ashkenazi, V. "Coordinate systems: How to get your position very precise and completely wrong." The Journal of Navigation 39.2 (1986): 269-278.
- [Atsushi and Sugimoto, 1994] Minato, Atsushi, and N. Sugimoto. "Method of measuring dihedral angles of a cube-corner retroreflector having curved mirror surfaces." Opt. Eng 33 (1994): 1187-1192.
- [Bartels et al., 2022] N. Bartels, P. Allenspacher, D. Hampf, B. Heidenreich, D. Keil, E. Schafer and W. Riede, "Space object identification via polarimetric satellite laser ranging." Commun Eng 1, 5 (2022). <https://doi.org/10.1038/s44172-022-00003-w>
- [BEV, 2024] Bundesamt für Eich- und Vermessungswesen, "International Terrestrial Reference System ITRS", 2021, Accessed 19.09.2024, Available: <https://transformator.bev.gv.at/at.gv.bev.transformator/wik>
- [Bombardelli and Pelaez, 2011] C. Bombardelli, J. Pelaez, IBS for contactless space debris removal, J. Guid. Contr. Dynam. 34 (3) (2011) 916e920, <https://doi.org/10.2514/1.51832>
- [Bonnal et al., 2013] Christophe Bonnal, Jean-Marc Ruault, Marie-Christine Desjean, Active debris removal: recent progress and current trends, Acta Astronaut. 85 (2013) 51e60, <https://doi.org/10.1016/j.actaastro.2012.11.009>.
- [Buller and Collins, 2009] Buller, G. S., and R. J. Collins. "Single-photon generation and detection." Measurement Science and Technology 21.1 (2009): 012002.
- [CDDIS, 2024] Crustal Dynamics Data Information System, NASA, Accessed: Oct. 2024, URL: https://cddis.nasa.gov/Data_and_Derived_Products/CDDIS_Archive_Access.html
- [ClearSpace, 2024] "A mission to make space sustainable," ClearSpace, Available: <https://clearspace.today/>.

- [Deghuria et al., 2023] Deghuria, A., Debnath, R., Varsha, G. and Raheja, K. "Recent Advances in Space Debris Removal Techniques; A study.", 2023.
- [Degnan, 1993] Degnan, John. Millimeter Accuracy Satellite Laser Ranging: A Review. 10.1029/GD025p0133. (1993)
- [Degnan, 2012] Degnan, J. J.: A tutorial on retro reflectors and arrays for SLR. In: ILRSWorkshop, Frascati, Italy (2012)
- [Dmytryszyn et al., 2021] Dmytryszyn, Mark, Matthew Crook, and Timothy Sands. "Lasers for satellite uplinks and downlinks." Sci 3.1 (2021): 4.
- [eoPortal, 2012] eoPortal, "ADEOS (Advanced Earth Observing Satellite) / Midori" [online] Available at: <https://www.eoportal.org/satellite-missions/adeos> [Accessed October 2024].
- [ESA, 2023] "The zero debris charter," European Space Agency Available: https://www.esa.int/Space_Safety/Clean_Space/The_Zero_Debris_Charter.
- [ESA, 2024] "Space debris by the numbers," ESA, Available: https://www.esa.int/Space_Safety/Space_Debris/Space_debris_by_the_numbers.
- [ESA, 2024] "ESA Space Debris Office," ESA Available: https://www.esa.int/Enabling_Support/Operations/Ground_Systems_Engineering/ESA_Space_Debris_Office.
- [Georges III, 1998] James A. Georges III, G. Charmaine Gilbreath, Peter B. Bolsma, Robert A. Kessel: Development of a Laser Ranging Target Optimized for LEO Spacecraft. Presented at the 11th International Workshop on Laser Ranging (1998)
- [Grunwaldt et al., 2016] Grunwaldt, L., Neubert, R., Barschke, M.F.: Optical tests of a large number of small COTS cubes. In: Presented at the 20th International Workshop on Laser Ranging (2016)
- [Hakala et al., 2009] Hakala, P., Hjalmarsson, L., Hannikainen, D. C. and Muhli, P. "Light curve morphology study of UW CrB—evidence for a 5 d superorbital period." Monthly Notices of the Royal Astronomical Society 394.2 (2009): 892-899.
- [Harvey, 1996] Harvey, B., The new Russian space programme from competition to collaboration, John Wiley and Sons, Chichester, England, 1996.
- [Hofwimmer, 2021] Hofwimmer T., "Technosat attitude analysis applied to larger satellites" Master's Thesis, Karl-Franzens-Universität Graz, 2021
- [ILRS, 2024] ilrs.gsfc.nasa.gov. 2021. ILRS Home Page. [online] Available at: <https://ilrs.gsfc.nasa.gov> [Accessed October 2024].

- [Jassmin and Kodeary, 2013] Jassim, J. M., and A. K. Kodeary. Experimental Study of the Influence of Aerosol Particles on Link Range of Free Space Laser Communication System in Iraq. *Journal of Applied Electromagnetism* 15. 28-33. (2013)
- [Kessler and Cour-Palais, 1978] Kessler, D. J., and Cour-Palais, B. G., "Collision frequency of artificial satellites: The creation of a debris belt," *Journal of Geophysical Research: Space Physics*, vol. 83, Jun. 1978, pp. 2637–2646.
- [Kessler, 2009] Kessler, Donald J. (8 March 2009). "The Kessler Syndrome"
- [Khairallah, 2021] Khairallah, Nadim, and Zaher M. Kassas. "Ephemeris closed-loop tracking of LEO satellites with pseudorange and Doppler measurements." *Proceedings of the 34th international technical meeting of the satellite division of the Institute of Navigation (ION GNSS+ 2021)*. 2021.
- [Kirchner et al., 2013] Kirchner, G., Koidl, F., Friederich, F., Koller, A., Neubert, R., Buske, I. (2013). "Current Status and Advances in Satellite Laser Ranging," *Journal of Geodesy*, 87(6), 1-17.
- [Kramer, 2014] Kramer, H.J. (2014) TechnoSat / TubSat-12 (Technische Universität Berlin Nanosatellite -12). eoPortal. Available at: <https://www.eoportal.org/satellite-missions/technosat#references> (Accessed: 22 August 2024).
- [Liu et al., 2020] Liu, E., Yang, Y., and Yan, Y., "Spacecraft Attitude Tracking for space debris removal using adaptive fuzzy sliding mode control," *Aerospace Science and Technology*, vol. 107, Dec. 2020, p. 106310.
- [Mejía-Kaiser et al., 2006] Mejía-Kaiser, Martha, Taking Garbage Outside: The Geostationary Orbit and Graveyard Orbits (October 1, 2006). *Proceedings of the 49th IISL Colloquium on the Law of Outer Space*, Valencia, 2006, Available at SSRN: <https://ssrn.com/abstract=3350005>
- [Mejía-Kaiser, 2020] Mejía-Kaiser, M., "Space debris mitigation guidelines of the committee on the peaceful uses of outer space, United Nations," *The Geostationary Ring*, Jun. 2020, pp. 390–394.
- [Marzioli et al., 2019] P. Marzioli, A. Gianfermo, L. Frezza, D. Amadio, M. Acernese, L. Parisi, G. Cialone, M.G. Pancalli, E. Vestito, F. Curianò, N. Picci, F. Piergentili and F. Santoni "LED-based attitude reconstruction and back-up light communication: experimental applications for the LEDSAT CubeSat" 2019 IEEE 5th International Workshop on Metrology for AeroSpace (MetroAeroSpace), Turin, Italy, 2019, pp. 720-725, doi: 10.1109/MetroAeroSpace.2019.8869673.
- [Mayorova et al., 2021] Mayorova, V.I.; Shcheglov, G.A.; Stognii, M.V. "Analysis of the space debris objects nozzle capture dynamic processed by a telescopic robotic arm". *Acta Astronaut.* 2021, 187, 259–270.

- [McLaughlin and Milton, 1970] Green, Constance McLaughlin; Lomask, Milton (1970). Vanguard: A History. Scientific and Technical Information Division, National Aeronautics and Space Administration. pp. 283–287.
- [NASA, 1963] Ariel I: the First International Satellite. Washington, D.C.: NASA. 1963. SP-43
- [NASA, 2023] Garcia, M., "Astronauts Complete Spacewalk, Dragon Launch Moves to Nov. 7," NASA Blogs, Nov. 2023.
- [NASA, 2024] "Frequently Asked Questions", NASA Orbital Debris Program Office, Astromaterials Research & Exploration Science Available: <https://orbitaldebris.jsc.nasa.gov/faq>.
- [Noll, 2008] Noll, Carey. "SLR, GNSS, VLBI, and DORIS Networks: ILRS+ IGS+ IVS+ IDS." 16th International Workshop on Laser Ranging, Poznan, Poland. 2008.
- [N2YO, 2016] "ALOUETTE 1 (S-27)". N2YO.com. April 26, 2016. Retrieved February 1, 2024.
- [Phipps et al., 1988] Phipps, C. R., Turner, T. P., Harrison, R. F., York, G. W., Osborne, W. Z., Anderson, G. K., Corlis, X. F., Haynes, L. C., Steele, H. S., Spicochi, K. C., and King, T. R., "Impulse coupling to targets in vacuum by KRF, HF, and CO₂ single-pulse lasers," Journal of Applied Physics, vol. 64, Aug. 1988, pp. 1083–1096.
- [Priyant and Surekha, 2019] C. Priyant Mark, Surekha Kamath, Review of Active Space Debris Removal Methods, Space Policy, Volume 47, 2019, Pages 194-206, ISSN 0265-9646, <https://doi.org/10.1016/j.spacepol.2018.12.005>.
- [Sánchez Piedra et al., 2023] Sánchez Piedra, Manuel, Manuel Sanjurjo Rivo, and Manuel Catalán Morollón. "Orbit determination of space debris using radar, laser and optical measurements." 2nd NEO and Debris Detection Conference. 2023.
- [Sanmartin et al., 1993] J.R. Sanmartin, M. Martinez-Sanchez, E. Ahedo, Bare wire anodes for electro- dynamic tethers, J. Propul. Power 9 (3) (1993) 353e360, <https://doi.org/10.2514/3.23629>.
- [Schildknecht et al., 1997] T. Schildknecht, U. Hugentobler, A. Verdun, Optical observations of space debris with the Zimmerwald 1-meter telescope, Advances in Space Research, Volume 19, Issue 2, 1997, Pages 221-228, ISSN 0273-1177
- [Shan et al., 2019] Shan, M.; Guo, J.; Gill, E. "An analysis of the flexibility modeling of a net for space debris removal". Adv. Space Res. 2019, 65, 1083–1094.
- [Silha et al., 2015] Silha, J., Linder, E., Hager, M. and Schildknecht, T. "Optical light curve observations to determine attitude states of space debris." Proceedings of 30th

- International Symposium on Space Technology and Science, Kobe-Hyogo, Japan. 2015.
- [Solomon Jr. et al., 1991] Solomon Jr, Otis M. "PSD computations using Welch's method." NASA STI/Recon Technical Report N 92 (1991): 23584.
- [Statista, 2024] "Number of active satellites by year 1957-2022," Statista, Available: <https://www.statista.com/statistics/897719/number-of-active-satellites-by-year/>.
- [Steele et al., 2005] R. Steele, T. Dillon, P. Pandya and Y. Ventsov, "XML-based mobile agents," International Conference on Information Technology: Coding and Computing (ITCC'05) - Volume II, Las Vegas, NV, USA, 2005, pp. 42-48 Vol. 2, doi: 10.1109/ITCC.2005.302.
- [Stephenson, 2015] Philip C L Stephenson: Satellite Laser Ranging Photon-Budget Calculations for a Single Satellite Cornercube Retroreflector: Attitude Control Tolerance. National Security and ISR Division DST-Group-TR-3172 (2015)
- [Subirana, 2011] Subirana J., Zornoza J.M., Pajares H., "Reference Frames in GNSS", 2011
- [Tamaki and Tanaka, 2022] Tamaki, Y.; Tanaka, H. "Experimental study on penetration characteristics of metal harpoons with various tip shapes for capturing space debris". Adv. Space Res. Off. J. Comm. Space Res. 2022, 70, 310–323.
- [Thorpe, 2022] Thorpe, E., "Space debris removal: Importance, today's methods and innovative spacecrafts," Orbital Today Available: <https://shorturl.at/cgcw6>.
- [Tieber-Hubmann, 2024] Tieber-Hubmann, Cornelia. (2024). "Determining SLR predictions to track space debris objects", Technische Universität Graz. <https://doi.org/10.3217/W7MPT-JZR52>
- [Trummer, 2023] Trummer, Nadine. (2023) "Simulation and classification of space debris light curves", Universität Graz, URN: urn:nbn:at:at-ubg:1-193729
- [Tyagla, 2024] Tyahla, L.J. (ed.) (last modified 2024) SLR - Ground Segment, International Laser Ranging Service. Available at: <https://ilrs.gsfc.nasa.gov/technology/groundSegment/index.html#s1> (Accessed: 07 August 2024).
- [UNOOSA, 2024] "United NationsOffice for Outer Space Affairs," UNOOSA Available: <https://www.unoosa.org/>.
- [Vallado et al., 2006] Vallado, D., Crawford, P., Hujsak, R. and Kelso, T. S "Revisiting spacetrack report Nr. 3." AIAA/AAS Astrodynamics Specialist Conference and Exhibit. 2006.

- [Vallado and Cefola, 2012] Vallado, David A., and Paul J. Cefola. "Two-line element sets—practice and use." 63rd International Astronautical Congress, Naples, Italy. 2012.
- [Vallado, 2016] Vallado, D. A., J. H. Seago, and P. K. Seidelmann. "Implementation issues surrounding the new IAU reference systems for astrodynamics." 16th AAS/AIAA Space Flight Mechanics Conference (2006): 06-134.
- [VanderPlas, 2018] VanderPlas, Jacob T. "Understanding the lomb–scargle periodogram." *The Astrophysical Journal Supplement Series* 236.1 (2018): 16.
- [Wang, 2018] Wang, P., Almer, H., Kirchner, G., Koidl, F., Steindorfer, M.: kHz SLR Application on the Attitude Analysis of TechnoSat. In: Presented at the 21st International Workshop on Laser Ranging (Canberra, 2018)
- [Yun et al., 2018] He Yun et. Al., Development of a 170-mm hollow corner cube retroreflector for the future lunar laser ranging. (2018)
- [Zhao et al., 2017] Zhao, Y.; Huang, P.; Zhang, F. Dynamic modeling and Super-Twisting Sliding Mode Control for Tethered Space Robot. *Acta Astronaut.* 2017, 143, 310–321.
- [Zhou and Sing, 2013] Zhou, Hui, and Song Li. "Effect of structural recession on the performance of a satellite laser retroreflector." *Optical Engineering* 52.4 (2013): 043001-043001.
- [Zhou et al., 2019] Y. Zhou, L. Zhang, Y. Cao and Z. Wu, "Attitude Estimation and Geometry Reconstruction of Satellite Targets Based on ISAR Image Sequence Interpretation," in *IEEE Transactions on Aerospace and Electronic Systems*, vol. 55, no. 4, pp. 1698-1711, Aug. 2019, doi: 10.1109/TAES.2018.2875503.